Article:

Yang, K, Zhu, X, Colombera, L et al. (9 more authors) (2023) Sediment provenance and dispersal in the early Eocene Dongying Depression, Bohai Bay Basin, Eastern China: Evidence from detrital zircon geochronology, geochemistry and petrology. Sedimentary Geology, 454. 106453. ISSN 0037-0738

https://doi.org/10.1016/j.sedgeo.2023.106453

Sediment provenance and dispersal in the early Eocene Dongying Depression, Bohai Bay Basin, Eastern China: evidence from detrital zircon geochronology, geochemistry and petrology

Ke Yang[a, b, c], Xiaomin Zhu[a, b]*, Luca Colombera[d], Adam McArthur[c], Nigel P. Mountney[c], Shifa Zhu[a, b], Lei Jin[a, b], Tingting Shen[a, b], Huaiyu Yang[e], Hongkui Chen[a, b], Shuanghui Xie[a, b], Xuling Jin[a, b]

[a] *State Key Laboratory of Petroleum Resource and Prospecting, Beijing, 102249, China*

[b] *College of Geosciences, China University of Petroleum, Beijing, 102249, China*

[c] *Sedimentology Research Group, School of Earth and Environment, University of Leeds, Leeds, LS2 9JT, UK*

[d] *Department of Earth and Environmental Sciences, University of Pavia, Via Ferrata 1, 27100, Pavia, Italy*

[e] *Shengli OilField, SINOPEC, Dongying, Shandong, 257000, China*

*Corresponding author.

E-mail address: xmzhu@cup.edu.cn

Abstract

Comprehensive provenance studies of syn-rift basin fills are required to better understand possible sources of clastic detritus and sediment routing systems. The Eocene fill of the Bohai Bay Basin in eastern China represents a syn-rift succession, where subsurface datasets permit investigation of sediment sources and sinks. New detrital zircon U-Pb samples (441 detrital zircon grains) from six wells were combined with elemental geochemical analysis of siliciclastic sediment, sandstone petrography and palynology to investigate depositional ages and provenance. This study demonstrates the importance of integrating geochronometry, geochemistry, petrology and palynology datasets to fully unravel syn-rift sediment provenance and routing. Zircons of the Dongying Depression were derived principally from an active continental margin island-arc setting characterized by felsic acid magmas, and subordinately from a recycled orogenic belt. The Shicun and Binnan faults controlled the relationship between sediment routing systems and source areas, explaining spatial differences of provenance signals in the depression. The routing system around the Shicun fault is characterized by a dominance of late Paleozoic and Paleoproterozoic zircons and subordinate Mesozoic zircons. In contrast, increased Mesozoic zircons in samples from south of the Binnan fault provide evidence of Mesozoic magmatism in this area. The early Eocene sediments record the signal of early Cretaceous magmatism in the North China Craton, but lack a record of substantial syn-depositional magmatic activity since the Paleogene in the Dongying Depression. Zircons from early Cretaceous strata and pre-existing zircons from the Xing-Meng Orogenic Belt and Inner Mongolia paleo-uplift were transported to the Yanshan and Luxi areas together. These sediments entered the Dongying Depression in the early Eocene, following a period of recycling. In addition, a Precambrian basement signal indicates possible denudation of Neoarchean to Proterozoic rocks in the Luxi uplift and from the Binnan fault footwall. Overall, the provenance signals of the basin reflect zircon recycling from an Early Cretaceous succession, denudation of ancient magmatic rock masses and the absence of syn-sedimentary magmatism.

Keywords

Syn-rift basin

Felsic island arc source

Recycled zircons

3D-Multidimensional scaling

North China Craton

1. Introduction

Sediment routing systems in tectonically active settings are commonly complicated; tracking the fate of sediments from their source to their sink over geological time can be challenging (Caracciolo, 2020). Regional provenance studies seek to determine the following: (i) robust ages from complex sedimentary datasets; (ii) the source region(s) from which clastic detritus was derived; and (iii) the processes responsible for the formation and evolution of source areas and sediment routing systems within the context of one or more particular regional tectonic setting (Cawood et al., 2012; Saylor et al., 2018; Tan et al., 2018; Liu et al., 2020; Barham et al., 2020). Comprehensive studies of sediment provenance in ancient successions employ techniques in geomorphology, sedimentary geology and basin analysis to ascertain environmental signals that indicate mechanisms and pathways for the dispersal of sediments (e.g., Gawthorpe et al., 2000; Michael et al., 2013; Romans et al., 2016; Duller et al., 2019; Toby et al., 2019; Caracciolo et al., 2020). Provenance analysis has now developed as a rigorous and quantitative scientific discipline in its own right, which utilizes a combination of complementary techniques (Caracciolo, 2020). Notably, the analysis of detrital minerals with particular chemical and isotopic signatures is employed to reveal associations with potential source areas and with particular tectonic settings (Peyton and Carrapa, 2013; Gehrels, 2014; Owusu Agyemang et al., 2019; Gómez et al., 2021).

Due to their widespread occurrence in magmatic, metamorphic and sedimentary rocks (Yang et al., 2022), detrital zircons are commonly used to identify sediment provenance via analysis of a combination of zircon crystallization ages, Th/U values, cathodoluminescence-induced internal textures, and grain shapes (Augustsson et al., 2018; Tan et al., 2018; Peng et al., 2020; Wang et al., 2021a; Caracciolo et al., 2021). In a crystalline state, zircons are physically and chemically robust and their trace-element compositions reflect the rocks in which they crystallized (Andersen et al., 2022). The recognition of compositional differences in the detrital U-Pb age components of sedimentary sequences permits the identification of different provenance signals (Tyrrell et al., 2012; Franklin et al., 2019). High degrees of grain abrasion are characteristic of multiple cycles of sedimentary grain recycling, whereas pristine zircons tend to exhibit their original morphology (Kowal-Linka et al., 2022). The employment of multiple complementary dating methods, including geochronometry and low-temperature thermochronometry, enables the reconstruction of the tectonic history of a basin, which enhances the recognition of syntectonic provenance information (Thomson et al., 2017; Ge et al., 2018; Buelow et al., 2018; Bernet, 2019; Malusa and Fitzgerald, 2019a, b). In addition, these techniques provide evidence of the history of unroofing of tectonostratigraphic units in orogens, and of the evolution and modification of drainage systems and sediment-dispersal pathways in response to tectonic activity (Caracciolo, 2020). An integrated approach employing mineralogy, petrography and bulk-rock geochemistry is now increasingly being employed to reveal variations in sediment provenance, tectonic activity, paleoweathering and paleoclimate (Ge et al., 2019; Sallam and Wanas, 2019; Chen and Robertson, 2020; Wanas and Assal, 2021).

The Bohai Bay Basin has been extensively studied due to its high petroleum potential. Existing studies mostly employed detrital zircons, heavy minerals, lithofacies and 3D-seismic data to characterize the source-to-sink system of the basin (e.g., Du et al., 2017; Zhu et al., 2017; Wang et al., 2021b; Chen et al., 2022; Liu et al., 2023). Previous studies demonstrate that the proportion of zircons from Mesozoic, Early Proterozoic and Neoarchean in the Shahejie Formation sandstones is relatively large; these studies confirmed the contribution of Mesozoic magmas and Precambrian metamorphic basement to the provenance of the middle Eocene in Bohai Bay Basin (Liu et al., 2023). However, several knowledge gaps remain in our understanding of the tectono-sedimentary evolution of the Dongying Depression, especially in relation to the early Eocene source-to-sink sedimentary systems and sediment-provenance evolution. Here, we present new U-Pb ages from detrital zircon geochronology, geochemistry, petrography and palynology to investigate the sediment provenance and tectonic setting of early Eocene strata of the Dongying Depression, in the Bohai Bay Basin, Eastern China. The tectonic evolution of the Dongying Depression includes a major syn-rift stage during the Paleogene (~65.0 to 24.6 Ma) (Liu et al., 2018). A comprehensive study on the provenance of this syn-rift basin-fill succession is required to better understand the possible source(s) of sediments and their transport pathways during this period. Such a study provides evidence on source-to-sink system evolution in the Dongying Depression during the early development of a series of linked rift depocenters, and more precisely elucidates the sources of sediments, and further provides a wealth of information about the tectonic setting and the basin evolution. Furthermore, it provides a basis for better understanding the contribution of tectonic evolution and magmatism of the North China Craton to the provenance of the early Eocene rift basin in the Bohai Bay Basin.

The aim of this study is to explain and discuss the sedimentary provenance of the Dongying Depression during the early Eocene, in relation to ongoing basin evolution. Specific research objectives are as follows: (1) to reconstruct the possible early Eocene provenance of the Dongying Depression; (2) to determine the relationship between detrital zircon ages from the Dongying Depression and its surrounding source areas, so as to characterize the evolution of the source-to-sink system; (3) to analyze and discuss the causes of differences in source signals.

2. Geological setting

The Dongying Depression is located in the southern part of the Jiyang Sub-basin (JYSB), which is a petroliferous basin in the North China Craton. It covers an area of approximately 5,700 km^2 and is a major hydrocarbon province within the southeastern part of the Bohai Bay Basin (BBB) in eastern China (Fig. 1A, B). The northern part of the basin is located adjacent to the Yanshan fold belt (YSFB) and the eastern extension of the Central Asian Orogenic belt (the Xing-Meng Orogenic Belt (XMOB)) (Fig. 1A). The Dongying Depression is bordered by the Chengjiazhuang bulge to the north, the Qingcheng and Binxian bulges to the west, and the Luxi uplift and the Guangrao bulge to the south (Fig. 1B) (Meng et al., 2021). A series of NW-SE trending normal faults developed in the JYSB as a consequence of regional extension during the late Cretaceous. These faults controlled the structural framework and depositional history of the JYSB (Wu, 2013).

Previous studies (Qiu et al., 2015; Liang et al., 2016; Liu et al., 2017; Zhu et al., 2021) demonstrate that the tectonic evolution of the Jiyang Sub-basin comprised a major syn-rift stage during the Paleogene (~65.0 to 24.6 Ma), followed by a post-rift stage during the Neogene (~24.6 Ma to present). Liu et al. (2018) recalibrated the ages of biozones, rifting episodes, and paleoclimate stages within the BBB based on the astronomical time scale. Six sub-stages of basin evolution have been reconstructed: (i) incipient rifting, which occurred in the Paleocene to early Eocene (ca. 65-50.5 Ma: Ek1-2); (ii) a late-initial rifting episode in the early to middle Eocene (ca. 50.5-42 Ma: Es4); (iii) a sub-stage of enhanced subsidence associated with a climax in tectonic extension, during the middle Eocene (ca. 42.5-35.99 Ma: Es3); (iv) a compressive sub-stage rifting during the middle Eocene to early Oligocene (ca. 36-28.86 Ma: Es1-2); (v) waning of rifting in the main BBB during the Oligocene (32.8-24.6 Ma: Ed1-3);

(vi) a thermal subsidence sub-stage characterized by relative tectonic quiescence and stable sedimentation rates, which has persisted from the Miocene to the present (24.6-0 Ma: Ng-m, Qp) (Feng et al., 2016; He et al., 2017; Liu et al., 2018; Zhu et al., 2021).

Paleogene to Neogene sediments are widely distributed in the Dongying Depression, and can be divided into five formations; from bottom to top: (i) the Kongdian Formation (Ek) of Paleocene to early Eocene age (ca. 65-50.8 Ma); (ii) the Shahejie Formation (Es) of Eocene to Oligocene age (ca. 50.8-28.86 Ma); (iii) the Dongying Formation (Ed) of Oligocene age (ca. 28.86-23 Ma); (iv) the Guantao Formation (Ng) of Miocene age (ca. 23-5.1 Ma); (v) and the Minghuazhen Formation (Nm) of Pliocene age (ca. 5.1-2.1 Ma) (Liu and Wang, 2013; Liu et al., 2018). The samples collected in this paper are from the Lower 4^{th} member of the early Eocene Shahejie Formation (Es_4^L) of the Dongying Depression (Fig. 2). The examined stratigraphy is characterized by red clastic deposits of terrestrial origin, which record evidence of sedimentation in fluvial and shallow-lake systems (Fig. 2; He et al., 2017).

3. Data and methods

We report six new detrital zircon U-Pb age samples (441 detrital zircon grains) from sandstones of the Lower 4^{th} member of the Shahejie Formation in the Dongying Depression. (Table 1, Fig. 3). U-Pb dating and trace-element analyses of zircons were conducted at the State Key Laboratory of Geological Processes and Mineral Resources, China University of Geosciences, Wuhan. Experiments were performed on an Agilent 7900 ICP-MS instrument (Agilent Technology, Tokyo, Japan) in combination with an ArF excimer laser (λ = 193 nm) (Geolas HD, MicroLas Göttingen, Germany). All analyses were performed with a laser spot size of 32 μm, a repetition rate of 5 Hz and a fluence of 8 J/cm^2. Absolute concordance of $^{207}Pb/^{235}U$ and $^{206}Pb/^{238}U$ ages is uncommon; the most common approach to the discordance problem is to exclude points that fall outside an envelope around the concordia curve

(Andersen et al., 2019). Here, we applied a <10% discordance filter to the generated data. For detrital zircon grains older than 1,000 Ma, the apparent age of $^{207}Pb/^{206}Pb$ was adopted due to the large volume of radiogenic Pb; instead, for those younger than 1,000 Ma, the more reliable $^{206}Pb/^{238}U$ apparent age was adopted due to the lower content of measurable radiogenic Pb (Sircombe, 1999). We also collected mudstone samples from wells Gan113, W46 and Ln120 for elemental geochemical analysis, and sandstone samples from wells Gan113, Fan178 and Ln90 for petrological analysis (Fig. 1C). Trace-element analyses of mudstone samples were conducted at the Analytical Laboratory of BRIUG, Beijing. Experiments were performed on an NexION300D ICP-MS. The major-element analyses of mudstone samples were conducted at the State Key Laboratory of Petroleum Resource and Prospecting (China University of Petroleum, Beijing), and the experiments were performed on a Malvern Panalytical Axios^{mAX} X-ray fluorescence spectrometer. Data on sandstone petrography were collected from the Shengli oilfield. Additionally, palynology data from the Lower 4th member in well W46, from the Shengli Oilfield database, are used for identifying marker species of the Cenozoic strata. Palynology data was obtained from confidential oilfield operator reports, with standard procedures for palynological sample preparation and analysis (Wood et al., 1996).

To investigate similarities and differences in zircon U-Pb age, we have used the nonparametric two-sample Kolmogorov-Smirnov test (K-S test) and Multidimensional scaling (MDS). The K-S test is based on the K-S statistic, which is the maximum difference between the empirical cumulative distribution functions of two samples (Wissink et al., 2018), and is most sensitive to the region near the modes of the sample distributions, and less sensitive to their tails (Vermeesch, 2013). The probability (*p*-value) of the K-S test is commonly used to measure the homology of samples. For example, a p-value <0.05 correlates to a >95% confidence level that the two samples are not drawn from the same parent population. In addition, the maximum vertical difference between the cumulative curves is compared, providing a D-value (Guynn & Gehrels, 2010). High D-values and low *p*-values indicate that the observed difference between the two populations may be explained by distinct origins (Pereira et al., 2016).

Multidimensional scaling is a useful tool for evaluating the generalities of large datasets containing multiple components (Wissink et al., 2018); it allows determination of similarities between successions within the same domain and in a broader regional scale (Solís-Alulima et al., 2022). In the case of non-metric MDS, the solution is not found analytically but numerically. This is done by minimizing a so-called 'stress parameter' (Vermeesch et al., 2013). Age samples are represented as a point in MDS; the distances between these points linearly correlate with the dissimilarities between samples, especially in the low-stress MDS maps (Saylor et al., 2018). One simple but effective way to aid in the interpretation of MDS maps is to draw a solid line from each point in the configuration to its 'closest' neighbor in dissimilarity-space, and a dotted line to the second closest neighbor. Thus, MDS maps group samples with similar age spectra, and discriminate samples with different spectra; the final stress value between 0.05 and 0.1 can be used to evaluate the quality of the MDS fit through the 'Shepard Plot' (Vermeesch, 2013). Here, we use DZmds software to plot 3D-MDS of all samples (stress=0.08), and jointly analyze it with Kernel Density Estimation (KDE), to better constrain the similarities between the age successions within the Dongying Depression and in a broader regional perspective.

4. Results

4.1. Petrography and geochemistry of detrital zircons

A total of 441 zircon grains were analyzed from 6 samples of $\mathrm{E}s_{4}^{\mathrm{L}}$, yielding Th/U ratios of 0.02–

2.00 (Fig. 4A). Among them, the Th/U ratio of most zircon grains is greater than 0.1, and Th/U >0.4 accounts for 68.7%, representing the majority of studied grains (Fig. 4A). The zircon grains with Th/U ratios greater than 0.4 are concentrated in the 100-500 Ma, 1750-2000 Ma and 2500-2800 Ma range. Most zircons that yielded concordant ages are prismatic with well-developed oscillatory zoning, and distinct core and rim structures; these features suggest an igneous origin (Ramos-Vázquez et al., 2019; Tan et al., 2020). The shapes of the zircon grains range from subrounded to angular, and the zoning of the zircon grains range from clear to weak (Fig. 5). By contrast, a few Early Proterozoic zircons with Th/U less than 0.1 are evident; these are darker in color and exhibit weak oscillatory zoning or metamorphic accretion structures (Fig. 4B, C). Compared with the zircon grains within 1,750-2,800 Ma, the CL reflection of the Mesozoic and Paleozoic zircon grains is stronger and the oscillation zoning is clearer (Fig. 5), suggesting that the young zircons have a greater igneous affinity than the ancient ones. Well-rounded stubby grains (Fig. 5) can be observed in each sample, suggesting that they have undergone mechanical abrasion (Shaanan and Rosenbaum, 2018) In this work, the normalized pattern is characterized by a steeply rising slope from the LREE to the HREE with a positive Ce-anomaly and negative Eu-anomaly (Fig. 6).

4.2. Zircon U-Pb ages

Six detrital zircon samples were collected and analyzed from $Es4^L$ (Table 2). For analyses with ages younger than 1,000 Ma, we use the $^{206}Pb/^{238}U$ age, whereas for older ages we use the $^{207}Pb/^{206}Pb$ age. All of the ages are represented for visualization and comparison in Kernel Density Estimation plots (KDEs). Samples GW-1, LH-9, YL-3, LV-2, BD-9 and BX-8 from $Es4^L$ represent the early Eocene sedimentary units. All samples collected from the Dongying Depression show similar age spectra (Fig. 7).

Samples GW-1 and LH-9 are located on the east and west sides of the Shicun fault respectively (Fig. 1). Sample GW-1 contains zircon U-Pb ages varying from 133 Ma to 2,744 Ma, with five significant unimodal age peaks at ca. 144 Ma, 317 Ma, 365 Ma, 1,869 Ma, and 2,541 Ma (Fig. 7). There are 16 zircon ages from the late Paleozoic (252-419 Ma), accounting for 25% of all ages; these are mainly distributed from 260±3 to 403±4 Ma; Carboniferous and Permian zircons are dominant. There are 33 zircon grains from the Paleoproterozoic (1,600-2,500 Ma), accounting for 51.6% of all ages, mainly distributed from 1,683±26 Ma to 2,495±24 Ma (Table 2). Sample LH-9 contains zircon U-Pb ages varying from 138 Ma to 2,587 Ma, with five significant unimodal age peaks at ca. 268 Ma, 314 Ma, 442 Ma, 1,904 Ma and 2,537 Ma (Fig. 7). There are 24 zircon ages from the late Paleozoic (252-419 Ma), mainly distributed from 254±2 to 338±4 Ma (Carboniferous to Permian), and 22 zircon grains from the Paleoproterozoic (1,600-2,500 Ma), mainly distributed from 1,635±21 Ma to 2,496±21 Ma, accounting for the two largest proportions among 63 zircon grains (38.09% and 34.92%) (Table 2). The age distribution characteristics of these two samples are relatively consistent; notably, the Mesozoic signals are relatively weak compared to those in the other samples. Sample LH-9 has a weak early Paleozoic signal, which is not detected in sample GW-1.

Sample YL-3 comes from the west side of the Shicun fault, which is located in the central part of the Boxing Sag (Fig. 1). It contains zircon U-Pb ages varying from 125 Ma to 2,594 Ma, with the most significant unimodal age peaks at ca. 1,856 Ma. The number of early Proterozoic zircon grains is up to fifty, accounting for 67.57% and contributing to the single dominant age peak of the sample; by contrast, other age signals are relatively weak (Fig. 7; Table 2).

Sample LV-2 comes from the south side of the Binnan fault (Fig. 1). It contains zircon U-Pb ages varying from 127 Ma to 2,554 Ma, with seven significant unimodal age peaks at ca. 132 Ma, 177 Ma, 261 Ma, 299 Ma, 321 Ma, 1,806Ma and 2,527 Ma (Fig. 7). Late Paleozoic, early Proterozoic and Mesozoic ages dominate the age spectrum, accounting for 32.05%, 28.21% and 23.08% of readings, respectively (Table 2). Although the age group greater than 2,500 Ma accounts for the smallest proportion (14.1%) (Table 2), there is a single peak at ca. 2,527 Ma, indicating that the distribution of Neoarchean age groups is also recorded in this sample. Compared with the samples near the Shicun fault, sample LV-2 displays a larger number of age peaks, reflecting a more varied age signal.

Similar characteristics also appear in the other two samples in the northwest region. Samples BD-9 and BX-8 exhibit age spectrum distributions similar to that of LV-2. Specifically, the bandwidth of the Mesozoic and Paleozoic age spectra is broad, and a single peak is not observed, with age peaks occurring mainly at ca. 130 Ma, ca. 165 Ma, and 250-260 Ma. The proportion of Precambrian zircons presents double peaks in sample BD-9 and BX-8; however, the peak value of sample BX-8 is slightly lower than that of sample BD-9.

4.3. Element geochemistry

The trace-element contents of the studied sediments, including REEs, are presented in supplementary material 2. The shape of the REE pattern and the size of Eu anomaly are considered important indicators of sediment provenance (Basu et al., 2016; Bansal et al., 2018; Chen and Robertson, 2020; Wanas and Assal, 2021). The chondrite-normalized patterns of REEs for wells W46, Gan113 and Ln120 are shown in Fig. 8. The REE values show enriched light REEs (LREEs) and low heavy REEs (HREEs). The Eu/Eu* and Ce/Ce* anomalies were quantified as follows: $Eu/Eu^*=2\times Eu_N/(Sm_N+Gd_N)$, $Ce/Ce^*=2\times Ce_N/(La_N+Pr_N)$ (Taylor and McLennan, 1985). The subscript N denotes the chondrite-normalized values according to Taylor and McLennan (1985). The chondrite-normalized La_N/Yb_N ratios are reported in supplementary material 2.

The total concentration of rare earth elements (ΣREE) shows significant variability from 190.87 ppm to 362.35 ppm (average = 252.59 ppm). The LREE content varies between 172.44 ppm and 333.89 ppm (average = 230.02 ppm); the HREE content varies between 18.43 ppm and 28.46 ppm (average = 22.57 ppm). The LREE/HREE ratio varies from 8.39 to 11.73 (average = 10.18). The $(La/Yb)_N$ ratio, which expresses the fractionation of LREE and HREE, ranges from 8.99 to 14.55 (average = 11.72). The Eu/Eu* values generally show negative anomalies, and vary from 0.57 to 0.71 (average = 0.65) (Table 3). The Ce/Ce* anomaly varies from 0.85 to 1.00 (average = 0.96). The negative Eu anomalies observed in the majority of samples indicate that the sediments were derived from felsic source rocks (Ramos-Vázquez and Armstrong-Altrin, 2019; Jia et al., 2019).

The geochemical analysis of clastic sediments provides insight into provenance and tectonic setting (Marsaglia et al., 2016; Critelli, 2018; Garzanti, 2019; Chen and Robertson, 2020). The studied samples demonstrate a felsic source (Fig. 9A, B) based on the bivariate diagrams of Hf vs. La/Th (Floyd and Leveridge, 1987) and La/Sc vs. Co/Th (McLennan et al., 1993). Similarly, analysis of Zr/Sc vs. Th/Sc (McLennan et al., 1993) indicates that most of the studied samples demonstrate affinity with the upper continental crust (UCC) (Fig. 9C). A comparison of the La/Sc, Th/Sc and Cr/Th ratios of the Es4L siliciclastic sediments (taking values of 3.16, 0.9 and 6.25, respectively) with those of the upper continental crust (Table 3), indicates that the sandstones deposited during the early Eocene originated from felsic rocks. Based on SiO_2 vs. K_2O/Na_2O data, the majority of the samples are compatible with an origin from an active continental-margin setting, and to some degree also with an island-arc context (Fig. 9D). The major element ratios are reported in supplementary material 3.

4.4. Sandstone detrital modes

The sandstone samples have similar grain compositions and textures, which are mainly mediumto coarse-grained and characterized by argillaceous and carbonate cementation (Fig. 10). The samples from well Fan178 are dominated by quartz (48% on average) but also contain significant fractions of feldspar (27.9% on average) and lithic fragments (24.1% on average) (Fig. 10B). Samples from well Gan113 are also dominated by quartz but with lower content than samples from Fan178 (43.3% on average) and also contain abundant feldspar (35.6% on average) and lithic fragments (21.4% on average) (Fig. 10A). The content of quartz and feldspar in the samples taken from Well Ln90 is similar (37.7% and 35.5% on average), and the fraction of lithic fragments is slightly less than that of the former two (26.8% on average) (Fig. 10C). The quartz grains are mostly monocrystalline, generally with sub-angular to sub-rounded shape. The occurrence of common potassium feldspar and plagioclase in the clastic composition indicates that these sandstones were dominantly sourced from acidic intrusive rocks. In the Qt-F-L diagram, samples from well Fan178 are distributed in the 'dissected arc' and 'recycled orogen' fields, whereas other samples lie exclusively in the 'dissected arc' field (Fig. 10D), which is consistent with elemental geochemical indicators (Fig. 9D).

5. Discussion

5.1. Depositional ages and provenance of the detrital zircons

The youngest U-Pb ages of zircon grains in populations of detrital zircons are commonly used to constrain maximum depositional ages (MDAs) of stratigraphic units (Brown and Gehrels, 2007; Jones et al., 2009). Determination of MDAs in detrital zircon studies remains a valid approach, which has been employed in many recent studies (Bahlburg et al., 2020; Barrett et al., 2020; Sharman & Malkowski, 2020; Solís-Alulima et al., 2022). The majority of these studies used methods that were tested by Dickinson and Gehrels (2009), including: (i) calculation of the MDA by the youngest single grain (YSG); (ii) determination of the youngest age peak defined by two or more analyses (YPP); (iii) computation of the weighted mean average of the youngest cluster of two or more grains that overlap at 1-sigma or 2-sigma uncertainty (YC1σ and YC2σ) (Sharman and Malkowski, 2020).

The ages obtained from all samples are presented in Table 4 and discussed below. The youngest single zircon grain ages are concentrated in the Lower Cretaceous in all samples. By contrast, the grain age calculated at 1-sigma or 2-sigma of uncertainty are older than the YSG, especially in samples from the Boxing Sag and near the Shicun fault (Table 4). It is crucial to select a group of appropriate parameters to constrain the maximum sedimentary age for provenance analysis. Dickinson and Gehrels (2009) recommend a method that makes use of the youngest grain cluster at 2σ (YGC 2σ) because the resulting MDAs are virtually never younger than the known biostratigraphic ages, unlike with YSG and youngest grain cluster at 1σ (YGC1σ). However, YSG is the most effective approach when the proportion of near-depositional-age grains is low (Coutts et al., 2019). Here, we choose the YSG for constraining the maximum depositional age in the early Eocene, since it is applicable to low-uncertainty and small datasets consisting of 50-120 samples (Jackson et al., 2004; Gehrels et al., 2008; Dickinson and Gehrels, 2009).

The presence of regional unconformities in the syn-rift stratigraphy is an important indicator of stratigraphic age division. A prior study showed that two important sequence boundaries can be identified in the late Cretaceous/Paleocene of the Dongying Depression, which represent first-order and second-order unconformities, respectively, developed in response to tectonic denudation at 65 Ma (Late Cretaceous/Paleocene) and 50.4 Ma (Kongdian Fm./the Lower 4th member of the Shahejie Fm.) (Meng and Ge, 2004).

In this study, palynology data were collected from well W46 for biostratigraphic constraints (Fig. 11). According to the species and genera of sporopollen, gymnosperms and angiosperms were relatively abundant in the Dongying Depression in the early Eocene. Among these, *Ephdripites trinata, Taxodiaceae pollenites, Qunercoidites potonie,* and *Ulmapollenites sp.* are dominant, which is consistent with the biostratigraphic time scale of the early Eocene in the Jiyang Depression, according to which the base of the Lower 4th member of the Shahejie Fm. is inferred to be 50.4 Ma (Wu et al., 2022). In contrast, the dominant Mesozoic species of the Bohai Bay Basin, namely *Cyathidites sp., Osmundacites sp., Cycadopites sp., Classopolli sp*. or *Classopollis sp.*, and *Abietinaeepollenites sp.*, are not found in our samples (Li et al., 2022). Thus, all the calculated MDAs are older than the true accumulation age (TDA) of the early Eocene sediments of the Dongying Depression. The lower limit of the depositional age of the early Eocene sediments in our study area is the Early Cretaceous. The changes in the MDA correlate with a change in the population that dominates the zircon age spectra (Orrillo et al., 2019).

Likewise, an important difference is seen in age distribution of the smaller populations between the area near the Shicun fault and the northwest belt of the Dongying Depression (Fig. 7). Samples from the latter area yield subordinate age clusters including the Early Cretaceous, Early-Middle Jurassic, Carboniferous-Permian, Paleoproterozoic and Neoarchean, whereas minor populations from the area around the Shicun fault are concentrated in the Mesozoic and Neoarchean. Considering that Cenozoic zircon grains are totally absent from all collected samples, we infer that there has been no widespread syn-depositional magmatic activity since the Paleogene in the Dongying Depression.

The provenance of the detrital zircons, in terms of expected tectonic settings, can also be distinguished by the cumulative proportion of differences between the crystallization ages (CA) of individual zircon grains and the depositional ages (DA) of the sediment (Cawood et al., 2012). Sediments that formed in a convergent setting (e.g., island arc) generally have large percentages of zircons with crystallization ages that are close to the depositional age of the sediments. By contrast, sediments deposited in collisional and extensional settings tend to have large percentages of zircons with crystallization ages that are much older than the depositional age of the sediments (Cawood et al., 2012). Based on the detrital zircon age distribution, the MDA analysis and the cumulative proportion diagram, we concluded that detrital zircons age distributions, the MDA analysis and the cumulative proportion diagram are all consistent with deposition in an extensional setting (Fig. 12).

5.2. Statistical comparison of ages in the Dongying Depression

A comparison of age distributions (Fig. 13) between samples from the Dongying Depression was made using the Kolmogorov-Smirnov (K-S) test, in the manner it is applied to establish provenance characteristics based on U-Pb dates (Pereira et al., 2016; Pereira and Gama, 2021; Solís-Alulima et al., 2022).

$P<0.05$ indicates a 95% probability that the two samples are derived from different parent populations (Tan et al., 2018; Solís-Alulima et al., 2022). According to the distribution of sample P value, the K-S test of the six samples from the early Eocene of the Dongying Depression demonstrates evident zonation, particularly between the area near the Shicun fault (samples GW-1, LH-9, YL-3) and the northwest region (samples LV-2, BD-9, BX-8) (Fig. 14A). To explore the causes of this spatial variability, and to infer tectonic drivers of differential provenance signals, it is necessary to consider the characteristics of basin-controlling faults that were active during this period. Samples GW-1 and LH-9, from the eastern and western sides of the Shicun fault, exhibit high homology with each other ($D=0.197$; $P=0.152$), and their cumulative U-Pb age curves demonstrate a relatively close match for the Phanerozoic and Precambrian (Fig. 13). In addition, the proportion of Mesozoic zircons (9.4%) from samples around the Shicun fault is significantly different from that of other ages (path A and B) (Fig. 13B). According to previous studies, the Shicun fault has been active since the Mesozoic, and continued to be active in the Paleocene and early Eocene, resulting in the depression being divided into eastern and western sectors (Wu et al., 2012; Zhang et al., 2012). The footwall of the Shicun fault is the Guangrao bulge, which formed after the Yanshan orogenesis in the Mesozoic (Han et al., 2011). It is inferred that the rift-related extension experienced by the Shicun fault in the early Eocene provided conditions for syn-depositional topographic development on both sides of the fault (He et al., 2017). The sediment dispersal pathways acting around the fault dominantly transported Carboniferous-Permian and Paleoproterozoic zircon particles.

Samples in the northwest region of the Dongying Depression constitute another group of data with high similarity; these samples were collected between the Gaoqing-Pingnan fault and the Binnan fault in the north. Wu et al. (2012) concluded that the slip-rate of the Binnan fault in the early Eocene was higher than that of the Gaoqing-Pingnan fault, and that the former had become the basin-bounding fault in the northern part of the depression in that period. Thus, the three samples located in the hanging wall of the Binnan fault are more likely to have incorporated the northern provenance system in this area (path C) (Fig. 14B). The D-value for samples LV-2 and BX-8 is the smallest, whereas their P-value is the largest, therefore, they form the pair of samples with the largest similarity in the collected dataset (D=0.096; P=0.835) (Fig. 14A). If sample BD-9 is compared with these two samples, it can be seen that their cumulative age distributions broadly coincide for the Mesozoic and Paleozoic interval (Fig. 13B). Some discrepancy is observed between the three cumulative age distributions in the Precambrian age interval (Fig. 13C); nonetheless, due to homogeneity in the Precambrian metamorphic basement preserved in the North China Craton, the Precambrian age curves of our samples are all inferred to record phases of Archean and Paleoproterozoic crustal evolution, cratonization and related geodynamic history (Yang et al., 2021).

The relative scarcity of Phanerozoic and Archean zircons is a key difference of sample YL-3 relative to the other samples (Fig. 7). A genetic relationship with sample GW-1 on the east side of the Shicun fault may be inferred, as their KDEs show that both samples contain zircon grains of similar age distributions. The cumulative U-Pb age curves of the two sample only coincide at ca. 150-300 Ma and ca. 1,850-1,860 Ma, and the Paleoproterozoic and late Paleozoic zircons represent the vast majority (67.57% and 16.22%, respectively) of sample YL-3. Sample YL-3 inherits the characteristics of the general lack of Mesozoic provenance signals on the eastern side of the Shicun fault, while retaining a record of the Precambrian metamorphic basement source. The activity of the Gaoqing-Pingnan and Shicun faults provided accommodation for sediment coming from the northern potential source area to the south. Therefore, it is possible that the northern sediment dispersal pathway continued beyond the fault slope into the periphery of the Boxing depression and along the Shicun fault (path D) (Fig. 14B); this may explain the similarity between sample LH-9 and the northwest sample.

5.3. Comparison with potential regional source areas

As described above, there are significant differences in the zircon signal carried by different sediment dispersal pathways in the early Eocene of the Dongying Depression. Therefore, in addition to the chronological analysis of the samples in the study area, we compare the age of the samples with previously published Paleozoic and Mesozoic U-Pb ages from samples from the surrounding areas, including the Luxi uplift and the Yanshan fold belt. This is done to explore the potential regional differences in sediment provenance in our study area during the early Eocene. Xu et al (2013, 2015) reported the characteristics of Mesozoic detrital zircons from the Luxi area, including their samples SD026-2, SD089-1 and SD092-1, which were collected from the Lower Cretaceous Mengyin Formation and the Middle-Upper Jurassic Santai Formation, with youngest U-Pb ages of 144.6 ± 4.1 Ma, 155 ± 1

Ma and 154 ± 7 Ma, respectively. Detrital zircon samples FW04-122, FW04-121 and 05FW003 are collected from the late Triassic-Early Cretaceous sandstone and Carboniferous-late Permian sandstone, in the Yanshan fold belt of the northern North China Craton (NCC). These samples indicate two apparently sudden shifts in source provenance between the NCC and Xing-Meng Orogenic Belt (XMOB), from the Late Triassic or earlier to the Late Jurassic (Yang et al., 2006).

The 3D-MDS shows that the data points from the early Eocene in the Dongying Depression are related to those from the Luxi area and the Yanshan fold belt to varying degrees, and are distributed differently in the three-dimensional space, allowing separation of data into three groups (Fig. 15).

The sediment distributed around the Shicun fault (path A) contains detrital zircons of Middle-Upper Jurassic sandstones from the Luxi uplift and of late Paleozoic sandstones from the Yanshan area (Group 1) (Fig. 15). In contrast, the age composition of sample LH-9 is more similar to the source of late Paleozoic detrital zircons of the Yanshan area. The results of the multi-sample comparison support the idea that the sediment routing system on the eastern side of the Shicun fault share some similarities with the source of the Jurassic detrital zircons of the Luxi uplift (Group 2) (Fig. 15). The northern routing systems labelled as C and D in Fig. 14B, which were controlled by the Binnan fault, are similar to the late Triassic-Early Cretaceous detrital zircon sources of the Yanshan fold belt, in which samples LV-2 and BX-8 are the closest and most closely related to samples FW04-121 (Group 3) (Fig. 15).

The maximum sedimentary age from the YSG indicates that the detrital zircons transported into the Dongying Depression in the early Eocene could not have been initially deposited earlier than the Early Cretaceous. In addition to spatial variability in fault activity as a control on the sediment routing system, the Early Cretaceous regional magmatic activity in the Luxi and Yanshan regions may also account for the difference in zircon source. This includes not only the syn-sedimentary zircons of the

Early Cretaceous, but also recycling of the pre-existing zircons, because the last source contributing zircons to a sedimentary cycle also contains a zircon family derived from early proto-sources (Gehrels, 2014).

To investigate this hypothesis, we compared the Mesozoic age signal of the early Eocene in the Dongying Depression with the magmatic intrusive signal in the Yanshan area (Fig. 16). The comparison shows that the bimodal ages of samples LV-2 and BX-8 in the Mesozoic correspond to the Early Cretaceous and Jurassic magmatic activities of the North China craton (Zhang et al., 2022); the age peaks are consistent with the two intrusion peaks in the Mesozoic (Fig. 16A). However, the Jurassic magmatic activity recorded by sample LV-2 and BX-8 is slightly different. The age peak of the former, at 177 Ma, is consistent with the timing of Early Jurassic magmatic intrusion in the Yanshan area, whereas ages of 160 Ma and 169 Ma in the latter are consistent with the peak time of Middle-Late Jurassic magmatic activity (Zhang et al., 2022). Qiu et al. (2023) concluded that the Jurassic intrusive rocks occurring in the Yanshan area are mainly granites, monzogranites, and syenites. Combined with the above-mentioned geochemical discrimination indicators (Fig. 9), we infer that our provenance signals are compatible with the Mesozoic acid magmatic rocks that were preset in the Yanshan area, and with Mesozoic rocks that were widely exposed along the northwestern routing system. In contrast, the Mesozoic magma signal has less influence on samples GW-1, LH-9 and YL-3.

Xu et al. (2013, 2015) confirmed that the Xing-Meng Orogenic Belt (XMOB) on the northern margin of the NCC transported zircon grains from north to the Yanshan region and the Luxi region during the Jurassic and Cretaceous. These zircons include not only the contemporaneous magmatic signals, but also signals of older recycled zircons. Specifically, the late Paleozoic age peak recorded in the Shicun fault sediment routing system is very synchronous, corresponding to the late Carboniferous single-peak magmatism (~315 Ma) of the Inner Mongolia Paleo-Uplift (IMPU). These zircons are believed to come from the IMPU in the context of an Andes-type magmatic arc setting, and correspond to the first uplift stage of the IMPU (325-312 Ma) (Zhang et al., 2009). This inference is consistent with the active continental-margin setting indicated by data on major elements (Fig. 9D) and with the dissected arc setting suggested by the sandstone petrography (Fig. 10). The routing system of the northwest provenance system in the early Eocene recorded the magmatism more fully after the first and second uplift phases of the IMPU (~271 Ma) (Ma et al., 2014) (Fig. 16B). The multiple exhumation phases of the IMPU in the late Paleozoic (Ma et al., 2014) facilitated the denudation of the magmatic body that supplied sediment to the NCC from north to south (Li et al., 2010). With regards to the Yanshan fold belt, Yang et al. (2006) argued that the provenance of the Paleozoic Shuangquan Formation in the Yanshan fold belt came from the NCC, whereas the Mesozoic Xingshikou and Xiayaopo sandstone samples recorded a mixing of XMOB and NCC sources. The two uplift events at ca. 158 and 137 Ma of the Yanshan orogeny (Yang et al., 2006) (Fig. 16A) facilitated the recycling of the pre-existing zircons. Together with the Mesozoic zircons from the XMOB, zircons were transported southward to the Luxi region, forming the material basis for the source of the Cenozoic Dongying Depression.

Notably, a small amount of zircons of Ordovician to Early Silurian age can be identified in our samples (442 Ma of sample LH-9, 434 Ma of sample YL-3, and 446 Ma of sample BD-9)(Fig. 7). These age peaks are consistent with the weighted mean ages of the Early Paleozoic igneous rocks from the Bainaimiao arc in the northern margin of the North China Craton. This reflects both the contribution of the felsic sources from the Early Palaeozoic Bainaimiao Arc (Eizenhöfer and Zhao, 2018), and the original source of Early Paleozoic zircons in the Boxing Sag and south of the Binnan fault. The origin of the zircons can therefore be ascribed to the continuous subduction and mature arc development that took place during ~455-415 Ma (Chen et al., 2020a).

By contrast, Neoarchean to early Proterozoic zircons from the Precambrian basement of the North China Craton are present in all samples in the study area, with the main age groups between 1.80-2.50 Ga, and Neoarchean peaks mainly at 2.52-2.57Ga. The NCC (including the Luxi area and the Yanshan fold belt) and the Inner Mongolia Paleo-Uplift (IMPU) are all characterized by the widespread presence of high-grade Archean to Paleoproterozoic metallic rocks (Ma et al., 2014; Xu et al., 2015; Tang et al., 2021; Yang et al., 2021). Previous studies have indicated that the late Archean micro-continental collision was an important process for crustal reworking and maturation of Archean upper continental crust of the NCC (Wang et al., 2022), and that the 2.50–2.42 Ga magmatism bore a recorded of a tectonic transition from subduction-collision to post-collisional extension during the Neoarchean cratonization (Zhou and Zhai., 2022; Zhai et al., 2021). By contrast, Xu and Liu (2019) propose that the ~2000-1895 Ma collisional orogeny and the ~1875-1850 Ma postcollisional extension played a crucial role in the early Proterozoic tectonic evolution of the NCC. Based on the cumulative proportion of differences between the crystallization ages (CA) of individual zircon grains and the depositional ages (DA) presented in section 5.1 (Fig. 12), we conclude that the Neoarchean to Early Proterozoic zircons in our samples likely record the transition from micro-continental collision to post-collisional extension in the NCC. In our samples, the shapes of the zircon grains range from sub-rounded to angular, and the Precambrian terranes (such as the Luxi uplift) were widely exposed around the Dongying depression in the early Eocene. Thus, there may have been two sources of Precambrian zircons for the early Eocene sandstone: one associated with denudation of the Precambrian rocks around the Luxi uplift and the Binnan fault, and a second one due to re-cycling of pre-existing zircons driven by the NCC orogeny in the late Paleozoic and Mesozoic (such as IMPU and YSFB).

5.4. The early Eocene provenance system of the Dongying Depression

The Luxi uplift and the Yanshan fold belt are the potential provenance areas of the early Eocene sediments of the Dongying Depression. The youngest zircon age in the sample indicates that the early Eocene detrital zircons in the Dongying Depression came from the denudation of Early Cretaceous detritus and lacked the direct influence of the early Eocene magmatic activity. The activity of the Shicun, Gaoqing-Pingnan and Binnan faults controlled the pathways of the sediment routing system. Due to the activity of the Gaoqing-Pingnan fault, the clastic materials shed from the Luxi uplift on the southern side were prevented from reaching the northwest region, and thus formed their own independent sediment routing system, along the area on the north side of the fault (Fig. 14B).

The southern routing system was mainly located in the vicinity of the Shicun fault. Although the fault had started to be active in the early Eocene, this study shows that fault activity did not lead to differences in the zircon signals on its eastern and western sides, which both demonstrate well-preserved late Paleozoic and early Proterozoic zircons (Fig. 17A). However, the Mesozoic age signal is significantly weaker than the northern provenance system (Fig. 17B). On the contrary, the routing system controlled by the Binnan fault on the northern side is characterized by a stronger magmatic signal related to Early Jurassic to Early Cretaceous volcanism in the Yanshan area. This contrasts markedly with what observed in the area near the Shicun fault (Fig. 17A-B). Previous research on the source-to-sink system of the Paleogene in the Bohai Bay Basin has identified that a considerable proportion of Mesozoic age populations, thought to indicate that the drainage system, could either (i) pass through the adjacent Jurassic and Cretaceous intrusive rocks, or (ii) traverse late Mesozoic clastic successions recording the early Mesozoic magmatic event in their detrital zircons (Tan et al., 2018).

In addition, the Boxing Sag was subject to an increased influx of recycled zircons in the early

Eocene compared with the periphery of the Shicun fault and the area south of the Binnan fault; this had a significant impact on differences in the distribution of zircon ages in the study area. Moreover, the record of late Paleozoic XMOB and IMPU magmatism is also a factor leading to differences in the routing system between the north and the south. This is mainly reflected in the fact that the late Paleozoic magmatic signal retained by the Luxi provenance system (Path A) in the south is recorded by a single peak, unlike the one in the north (Fig. 17A). There is relatively little difference between the two types of routing systems with respect to their record of Neoarchean-Paleoproterozoic magmatic-metamorphic signals related to the NCC.

Notably, in this study, we observe that the age components of the sediments in the Dongying Depression of the early Eocene have different degrees of affinity with the Yanshan and Luxi areas, but the zircon age spectrum in the hinterland is not fully consistent with the age signals of the provenance areas (Fig. 17A). In general, the loss or redistribution of U-Pb age components is a common phenomenon in source-to-sink systems, since these may reflect variations in sediment flux in response to climatic and tectonic controls affecting the drainage systems (Chen et al., 2020b; Caracciolo, 2020). However, not all changes in zircon grain populations are associated with dramatic changes of drainages in the hinterland (Chen et al., 2020b). Lamminen et al. (2015) suggest that changes of zircon age suites are all related to one another, with any decrease or increase in any one age suite inducing a corresponding increase or decrease in other age suites; this may also be a reason for differences in source signals in our study area. Therefore, based on the above results, we tentatively interpret an overall consistency in the feeder systems supplying zircons to the Dongying Depression from the Yanshan fold belt and Luxi uplift during the early Eocene.

6. Conclusions

This study investigated 441 detrital zircon grains from early Eocene aged sediments from the Dongying Depression with respect to their grain morphology, isotopic composition, and associated mudstone elementary geochemistry.

(1) The peak zircon ages of the samples mainly show Mesozoic, late Paleozoic, early Proterozoic and Neoarchean affinities. The Maximum Depositional Ages (MDAs) of detrital zircons recovered from the Eocene interval of the Dongying Depression mostly indicate a Lower Cretaceous MDA, indicating that there has been no large-scale syn-depositional magmatic activity since the Paleogene in the Dongying Depression. The ancient ages recorded in zircons comes from the direct erosion of the parent rock and also likely to be derived from recycling.

(2) The chronological data comparison based on the K-S test shows that there were two main provenance areas for sediments in the Dongying Depression during the early Eocene. One routing system was mainly located around the Shicun fault, and was controlled by the activity of this fault, the Gaoqing-Pingnan fault and the Binnan fault; the second routing system was located on the south side of the Binnan fault. The routing system around the Shicun fault is mainly characterized by a lack of Mesozoic zircons, and late Paleozoic and Paleoproterozoic zircons are relatively concentrated. The proportion of Jurassic and Early Cretaceous zircons is significantly higher in the southern routing system of the Binnan fault, in which zircons of late Paleozoic and Precambrian age are also widely recorded. Through multi-comparison with the results of geochronometry in the surrounding areas, it is found that the Luxi uplift and Yanshan fold belt were the source areas of the sediments. The provenance system controlled by the Binnan fault is closely related to the Early Cretaceous magmatism of the Yanshan fold belt, whereas the Luxi area generally lacks such

records.

(3) Carboniferous to Permian and Neoarchean to Paleoproterozoic zircons are generally preserved in the early Eocene sediments of the Dongying Depression. These zircons are recorded from the magmatism of the Xing-Meng Orogenic Belt and the Mongolia Paleo-Uplift in the late Paleozoic and the Precambrian metamorphic basement of the North China Craton. The smaller amount of Early Paleozoic zircons reflects the contribution of felsic sources from the Bainaimiao Arc on the northern margin of the North China Craton.

(4) In the absence of syn-depositional magmatism, the age signal in the Bohai Bay Basin is the result of recycled zircons from sedimentary rocks and denudation of pre-existing magmatic rock masses. These recycled signals are faithful records of all major magmatic-metamorphic events in the orogenic belts around the Bohai Bay Basin. The activity of syn-depositional faults controls the relationship between sediment routing systems and source areas, and explains the spatial difference of provenance signals in the Bohai Bay Basin.

Acknowledgements

This work was supported by the National Natural Science Foundation of China (No.42272110). We would like to acknowledge the Geoscience Institute of the Shengli Oilfield (SINOPEC) for unlimited access to their core samples, palynology and well data. We gratefully acknowledge the State Key Laboratory of Geological Processes and Mineral Resources (China University of Geosciences, Wuhan) for their help of LA-MC-ICP-MS analyses. Thanks to the State Key Laboratory of Petroleum Resource and Prospecting (China University of Petroleum, Beijing) and the Analytical Laboratory of BRIUG, Beijing for providing support for geochemical testing. We thank Dr. Hang Cui, Wenyu Wang and Chaofan Wan for their help with the petrological analysis.

References

Andersen, T., Elburg, M.A., Magwaza, B.N., 2019. Sources of bias in detrital zircon geochronology: Discordance, concealed lead loss and common lead correction. Earth-Science Reviews 197, 102899. https://doi.org/10.1016/j.earscirev.2019.102899.

Andersen, T., Niekerk, H. V., Elburg, M. A., 2022. Detrital zircon in an active sedimentary recycling system: Challenging the 'source-to-sink' approach to zircon-based provenance analysis. Sedimentology 69, 2436–2462. https://doi.org/10.1111/sed.12996.

Augustsson, C., Voigt, T., Bernhart, K., Kreißler, M., Gaupp, R., Gärtner, A., Hofmann, M., Linnemann, U., 2018. Zircon size-age sorting and source-area effect: The German Triassic Buntsandstein Group. Sedimentary Geology 375, 218–231. https://doi.org/ 10.1016/j.sedgeo.2017.11.004.

Bahlburg, H., Zimmermann, U., Matos, R., Berndt, J., Jimenez, N. and Gerdes, A. 2020. The missing link of Rodinia breakup in western South America: A petrographical, geochemical, and zircon Pb-Hf isotope study of the volcanosedimentary Chilla beds (Altiplano, Bolivia). Geosphere 16, 619–645.

Bansal, U., Banerjee, S., Ruidas, D.K., Pande, K., 2018. Origin and geochemical characterization of the glauconites in the Upper Cretaceous Lameta Formation, Narmada Basin, central India. Journal of Palaeogeography 7, 99–116. https://doi.org/10.1016/j.jop.2017.12.001.

Barham, M., Kirkland, C. L., Hovikoski, J., Alsen P., Hollis J., Tyrrell S., 2020. Reduce or recycle? Revealing source to sink links through integrated zircon–feldspar provenance fingerprinting. Sedimentology 68, 531-556. https://doi.org/10.1111/sed.12790.

Barrett, P.M., Sciscio, L., Viglietti, P.A., Broderick, T.J., Suarez, C.A., Sharman, G.R., Jones, A.S., Munyikwa, D., Edwards, S.F., Chapelle, K.E.J., Dollman, K.N., Zondo, M., Choiniere, J.N., 2020. The age of the

Tashinga Formation (Karoo Supergroup) in the Mid-Zambezi Basin, Zimbabwe and the first phytosaur from mainland subSaharan Africa. Gondwana Research 81, 445–460.

Basu, A., Bickford, M.E., Deasy, R., 2016. Inferring tectonic provenance of siliciclastic rocks from their chemical compositions: a dissent. Sedimentary Geology 336, 26–35.

Bernet, M., 2019. Exhumation studies of mountain belts based on detrital fission track analysis on sand and sandstones. In: Fission-track thermochronology and its application to geology. Springer, Cham, pp. 269-277.

Brown, E.R., Gehrels, G.E., 2007. Detrital zircon constraints on terrane ages and affinities and timing of orogenic events in the San Juan Islands and North Cascades, Washington. Can. J. Earth Sci. 44, 1375–1396.

Buelow, E.K., Suriano, J., Mahoney, J.B., Kimbrough, D.L., Mescua, J.F., Giambiagi, L.B., Hoke, G.D., 2018. Sedimentologic and stratigraphic evolution of the Cacheuta basin: Constraints on the development of the Miocene retroarc foreland basin, south-central Andes. Lithosphere 10 (3), 366-391.

Caracciolo, L., Ravidà, D. C. G., Chew, D., Janßen, M., Lünsdorf, N. K., Heins, W. A., Stephan, T., Stollhofen, H., 2021. Reconstructing environmental signals across the Permian-Triassic boundary in the SE Germanic Basin: A Quantitative Provenance Analysis (QPA) approach. Global and Planetary Change 206, 103631. https://doi.org/10.1016/j.gloplacha.2021.103631.

Caracciolo, L., 2020. Sediment generation and sediment routing systems from a quantitative provenance analysis perspective: Review, application and future development. Earth-Science Reviews 209, 103226. https://doi.org/10.1016/j.earscirev.2020.103226.

Cawood, P.A., Hawkesworth, C., Dhuime, B., 2012. Detrital zircon record and tectonic setting. Geology 40, 875–878.

Chen, G., Robertson, A.H.F., 2020. User's guide to the interpretation of sandstones using whole-rock chemical data, exemplified by sandstones from Triassic to Miocene passive and active margin settings from the Southern Neotethys in Cyprus. Sedimentary Geology 400, 105616. https://doi.org/10.1016/j.sedgeo.2020.105616.

Chen, Y., Zhang, Z.C., Qian, X.Y., Li, J.F., Ji, Z.J., Wu, T.R., 2020a. Early to mid-Paleozoic magmatic and sedimentary records in the Bainaimiao Arc: An advancing subduction-induced terrane accretion along the northern margin of the North China Craton. Gondwana Research 79,263-282.

Chen, H., Zhu, X., Wood, L.J., Shi, R. 2020b. Evolution of drainage, sediment‐flux and fluvio‐deltaic sedimentary systems response in hanging wall depocentres in evolving non‐marine rift basins: Paleogene of Raoyang Sag, Bohai Bay Basin, China. Basin Res 32, 116–145.

Chen, H., Zhu, X., Gawthorpe, R.L., Wood, L.J., Liu, Q., Li, S., Shi, R., Li, H., 2022. The interactions of volcanism and clastic sedimentation in rift basins: insights from the Palaeogene-Neogene Shaleitian uplift and surrounding sub-basins, Bohai Bay Basin, China. Basin Res. 34 (3), 1084–1112.

Coutts, D. S., Matthews, W. A., Hubbard S M. 2019. Assessment of widely used methods to derive depositional ages from detrital zircon populations. Geoscience Frontiers 10, 1421-1435.

Critelli, S., 2018. Provenance of Mesozoic to Cenozoic circum-Mediterranean sandstones in relation to tectonic setting. Earth-Science Reviews 185, 624–648.

Cullers, R.L., 1994. The controls on the major and trace element variation of shales, siltstones, and sandstones of Pennsylvanian-Permian age from uplifted continental blocks in Colorado to platform sediment in Kansas, USA. Geochimica et Cosmochimica Acta 58, 4955–4972.

Cullers, R.L., 2000. The geochemistry of shales, siltstones and sandstones of Pennsylvanian-Permian age, Colorado, USA: implications for provenance and metamorphic studies. Lithos 51, 181–203.

Cullers, R.L., Podkovyrov, V.N., 2000. Geochemistry of the Mesoproterozoic Lakhanda shales in southeastern Yakutia, Russia: implications for mineralogical and provenance control, and recycling. Precambrian Research 104, 77–93.

Dickinson, W.R., 1985. Interpreting provenance relations from detrital modes of sandstones. In: Zuffa, G.G. (Ed.), Provenance of arenites. Reidel, Dordrecht, NATO ASI Series 148, 333–361.

Dickinson, W.R., Gehrels, G.E., 2009. U-Pb ages of detrital zircons in Jurassic eolian and associated sandstones of the Colorado pLateau: evidence for transcontinental dispersal and intraregional recycling of sediment. GSA Bulletin 121,408-433.

Du X., Xu C., Pang X., Wang Q., Wang Q., Zhao M. 2017. Quantitative reconstruction of source-to-sink systems of the first and second members of the Shahejie Formation of the Eastern Shijiutuo uplift, Bohai Bay Basin, China. Interpretation, 5 (4): ST85-ST102. https://doi.org/10.1190/INT-2017-0029.1

Duller, R. A., Armitage, J. J., Manners, H. R., Grimes, S. T., Jones, T. D. 2019. Delayed sedimentary response to abrupt climate change at the Paleocene-Eocene boundary, northern Spain. Geology 47, 159–162.

Eizenhöfer, P.R., Zhao, G., 2018. Solonker Suture in East Asia and its bearing on the final closure of the eastern segment of the Palaeo-Asian Ocean. Earth-Sci. Rev. 186, 153-172.

Feng, Y. L., Jiang, S., Hu, S. Y., Li, S. T., Lin, C. S., Xie, X. N., 2016. Sequence stratigraphy and importance of syndepositional structural slope-break for architecture of Paleogene syn-rift lacustrine strata, Bohai Bay Basin, E. China. Marine and Petroleum Geology 69, 183-204.

Floyd, P.A., Leveridge, B.E., 1987. Tectonic environment of the Devonian Gramscatho basin, south

Cornwall: framework mode and geochemical evidence from turbiditic sandstones. Journal of the Geological Society of London 144, 531–542.

Franklin, J., Tyrrell, S., Morton, A.C., Frei, D., Mark, C., 2019. Triassic sand supply to the Slyne Basin, offshore western Ireland e new insights from a multi-proxy provenance approach. Journal of the Geological Society 176, 1120-1135.

Gawthorpe, R.L., Leeder, M.R., 2000. Tectono-sedimentary evolution of active extensional basins. Basin Res. 12, 195–218.

Garzanti, E., 2019. Petrographic classification of sand and sandstone. Earth-Science Reviews 192, 545–563.

Ge, J. W., Zhu, X. M., Wang, R., Jones, B. G., Chen, W. C. 2018. Tectono-sedimentary evolution and hydrocarbon reservoirs in the Early Cretaceous Tanan Depression, Tamtsag Basin, Mongolia. Marine and Petroleum Geology 94, 43-64.

Ge, X., Mou, C., Yu, Q., Liu, W., Men, X., He, J., 2019. The geochemistry of the sedimentary rocks from the Huadi No. 1 well in the Wufeng-Longmaxi formations (Upper Ordovician-Lower Silurian), South China, with implications for paleoweathering, provenance, tectonic setting and paleoclimate. Marine and Petroleum Geology 103, 646–660.

Gehrels, G.E., 2014. Detrital Zircon U-Pb geochronology applied to tectonics. Annu. Rev.Earth Planet Sci. 42, 127–149.

Gehrels, G.E., Valencia, V.A., Joaquin, R., 2008. Enhanced precision, accuracy, and efficiency, and spatial resolution of U-Pb ages by laser ablation-multicollector inductively coupled plasma-mass spectrometry. Geochemistry, Geophysics, Geosystems 9, 1-13.

Gómez, R., Galetto, A., Arzadún G., Tunik M., Casadio S., Parada M., Lothari L. 2021. Multiproxy provenance analysis of Lower to Upper Cretaceous synorogenic deposits in the Southern Andes (34-35S): Evidence of coeval volcanism during the onset of the Andean orogeny. Cretaceous Research 128, 104985. https://doi.org/10.1016/j.cretres.2021.104985

Guynn, J. and Gehrels, G. 2010. Comparison of Detrital Zircon Age Distributions Using the K-S Test. Arizona LaserChron Center. Available at: https://laserchron.org/

Han Z N. 2011. Study on the Reservoir Characteristics of Carbonate Buried Hill in Guangrao Oilfield. China University of Petroleum (Master Degree Thesis in Chinese with English Abstract).

He, J., Ding, W., Jiang, Z., Jiu, K., Li, A., Sun, Y., 2017. Mineralogical and chemical distribution of the Es3^{L} oil shale in the Jiyang Depression, Bohai Bay Basin (E China): implications for paleoenvironmental reconstruction and organic matter accumulation. Marine and Petroleum Geology 81, 196–219.

Jackson, S.E., Pearson, N.J., Griffin, W.L., Belousova, E.A., 2004. The application of laser ablation-inductively coupled plasma-mass spectrometry to in situ U-Pb zircon geochronology. Chemical Geology 221, 47-69.

Jia, X. L., Zhai, M. G., Xiao, W. J., Sun, Y, Ratheesh-Kumar, R. T, Yang, H., Zhou, K. F., Wu, J. L. 2019. Late Neoarchean to Early Paleoproterozoic tectonic evolution of the southern North China Craton: Evidence from geochemistry, zircon geochronology and Hf isotopes of felsic gneisses from the Taihua complex. Precambrian Research 326, 222-239.

Jones III, J.V., Connelly, J.N., Karlstrom, K.E., Williams, M.L., Doe, M.F., 2009. Age, provenance, and tectonic setting of Paleoproterozoic quartzite successions in the southwestern United States. Geol. Soc. Am. Bull 121, 247–264.

Kowal-Linka, M., Jastrzębski, M., Krzemińska, E., Czupyt, Z. 2022. The importance of parameter selection in studies of detrital zircon provenance: An example from Mesozoic deposits of the Bohemian Massif foreland (Poland). Palaeogeography, Palaeoclimatology, Palaeoecology 599, 111035. https://doi.org/10.1016/j.palaeo.2022.111035.

Lamminen, J., Andersen, T., & Nystuen, J. P. 2015. Provenance and rift basin architecture of the Neoproterozoic Hedmark Basin, South Norway inferred from U–Pb ages and Lu–Hf isotopes of conglomerate clasts and detrital zircons. Geological Magazine 152, 80–105.

Li, C., Chen, S. Y., Pu, X. G., Yang, H. Y., Hou, Z. S., Yan, J. H. 2022. Stratigraphic Subdivision and Correlation of the Mesozoic in the Bohai Bay Basin. Earth Science. doi:10.3799/dqkx.2022.220 (in Chinese with English abstract).

Li, H. Y., He, B., Xu, Y. G., Huang, X. L. 2010. U–Pb and Hf isotope analyses of detrital zircons from Late Paleozoic sediments: Insights into interactions of the North China Craton with surrounding plates. Journal of Asian Earth Sciences 39, 335-346.

Liang, J. T., Wang, H. L., Bai, Y., Ji, X. Y., Duo, X. M. 2016. Cenozoic tectonic evolution of the Bohai Bay Basin and its coupling relationship with Pacific PLate subduction. Journal of Asian Earth Sciences 127, 257-266.

Liu, C., Wang, P., 2013. The role of algal blooms in the formation of lacustrine petroleum source rocks-evidence from Jiyang depression, Bohai Gulf Rift Basin, eastern China. Palaeogeogr. Palaeoclimatol. Palaeoecol 388, 15–22.

Liu, E.T., Wang, H., Feng, Y. X., Pan, S. Q., Jing, Z. H., Ma, Q. L., Gan, H. J., Zhao, J. X. 2020. Sedimentary architecture and provenance analysis of a sublacustrine fan system in a half-graben rift depression of the South China Sea. Sedimentary Geology. 409, 105781. https://doi.org/10.1016/j.sedgeo.2020.105781

Liu, J. P., Xian, B. Z., Wang, J. H., Ji, Y. L., Lu, Z. Y., Liu, S. J., 2017. Sedimentary architecture of a sub-lacustrine debris fan: Eocene Dongying Depression, Bohai Bay Basin, east China. Sedimentary Geology 362, 66-82.

Liu Q., Zhu X., Zhou Z., Bao Y., Shi W. 2023. Provenance identification and source-to-sink studies from an intrabasinal subaqueous uplift in the Eocene western Bohai Bay Basin, eastern north China. Marine and Petroleum Geology, 149, 106087. https://doi.org/10.1016/j.marpetgeo.2022.106087

Liu, Z. H., Huang, C. J., Algeo, T. J., Liu, H. M., Hao, Y. Q., Du, X. B., Lu, Y. C., Chen, P., Guo, L. Y., Li, P. 2018. High-resolution astrochronological record for the Paleocene-Oligocene(66–23 Ma) from the rapidly subsiding Bohai Bay Basin, northeastern China. Palaeogeography, Palaeoclimatology, Palaeoecology 510, 78-92.

Ma, S.X., Meng, Q.R., Duan, L., Wu, G.L., 2014. Reconstructing Late Paleozoic exhumation history of the Inner Mongolia highland along the northern edge of the North China Craton. Journal of Asian Earth Sciences 87, 89–101.

Malusa, M.G., Fitzgerald, P.G., 2019a. From cooling to exhumation: setting the reference frame for the interpretation of thermochronologic data. In: Fission Track Thermochronology and its Application to Geology. Springer, Cham, pp. 147-164.

Malusa, M.G., Fitzgerald, P.G., 2019b. Application of thermochronology to geologic problems: bedrock and detrital approaches. In: Fission-Track Thermochronology and its Application to Geology. Springer, Cham, pp. 191-209.

Marsaglia, K.M., Barone, M., Critelli, S., Busby, C., Fackler-Adams, B., 2016. Petrography of volcaniclastic rocks in intra-arc volcano-bounded to fault-bounded basins of the Rosario segment of the Lower Cretaceous Alisitos oceanic arc, Baja California, Mexico. Sedimentary Geology 336, 138–146.

McLennan, S.M., Hemming, S., McDaniel, D.K., Hanson, G.N., 1993. Geochemical approaches to sedimentation, provenance, and tectonics. In: Johnsson, M.J., Basu, A. (Eds.), Processes Controlling the Composition of Clastic Sediments: Boulder, Colo rado. Geological Society of America, Special Paper vol. 284, pp. 21–40.

Meng, J. Y., Jiang, Z. X., Yang, Y. P., Nian, T., 2021. Soft-sediment deformation structures in a lacustrine depositional context: An example from the Eocene Dongying Depression in the Bohai Bay Basin, East China. Sedimentary Geology 426,106039. https://doi.org/10.1016/j.sedgeo.2021.106039.

Meng, X.H., Ge, R., 2004. China-Korea Sequence Stratigraphy, Events and Evolution. Science Press, Beijing pp. 535-539. (In Chinese with English Abstract).

Michael, N.A., Whittaker, A.C., Allen, P.A., 2013. The functioning of sediment routing systems using a mass balance approach: Example from the Eocene of the southern Pyrenees. Geology 121, 581–606.

Orrillo, J. M. P., Suárez, A.O., Rivarola, D., Otamendi, J. E., Morosini, A., Romero, R., Leisen, M., Barra, F. 2019. Depositional age and provenance in the San Luis Formation, Sierras Pampeanas, Argentina: Evidence from detrital zircon studies. Journal of South American Earth Sciences 94, 102228. https://doi.org/10.1016/j.jsames.2019.102228.

Owusu Agyemang, P.C., Roberts, E.M., Bussert, R., Evans, D., Müller, J., 2019. U-Pb detrital zircon constraints on the depositional age and provenance of the dinosaur-bearing Upper Cretaceous Wadi Milk Formation of Sudan. Cretaceous Research 97, 52-72.

Peng, Y., Zhang, Y., Xing, E., Wang, L., 2020. Provenance and tectonic significance of the Zhongwunongshan Group from the Zhongwunongshan Structural Belt in China: insights from zircon geochronology. Open Geosci 12, 25–43.

Pereira, M.F., Albardeiro, L., Gama, C., Chichorro, M., Hofmann, M., Linnemann, U., 2016. Provenance of Holocene beach sand in the Western Iberian margin: the use of the Kolmogorov-Smirnov test for the deciphering of sediment recycling in a modern coastal system. Sedimentology 63, 1149–1167.

Pereira, M.F., Gama, C., 2021. Revisiting the intermediate sediment repository concept applied to the provenance of zircon. Minerals 11, 233. https://doi.org/10.3390/ min11030233.

Peyton, L.S., Carrapa, B., 2013. An introduction to low-temperature thermochronologic techniques, methodology, and applications. In: Knight, C., Cuzella, J. (Eds.), Application of structural methods to Rocky Mountain hydrocarbon exploration and development: AAPG Studies in Geology 65, 15-36.

Qi, J. F., Yang, Q., Lu, K. Z., Zhou, J. X., Wang, Z. Y., 2004. Geologic map of sub-outcrop and its implied information of tectogenesis in Bohai Bay basin province. Earth Science Frontiers 11, 299-307. (In Chinese with English Abstract)

Qiu, N.S., Xu, W., Zuo, Y.H., Chang, J., 2015. Meso-Cenozoic thermal regime in the Bohai Bay Basin, eastern North China Craton. Internatioanal Geology Review 57 (3), 271–289.

Qiu,H.B., Lin, W., Chen, Y., Faure, M. 2023. Jurassic–Early Cretaceous tectonic evolution of the North China Craton and Yanshanian intracontinental orogeny in East Asia: New insights from a general review of stratigraphy, structures, and magmatism. Earth-Science Reviews 237, 104320. https://doi.org/10.1016/j.earscirev.2023.104320

Ramos-Vázquez, M. A., Armstrong-Altrin, J.S. 2019. Sediment chemistry and detrital zircon record in the Bosque and Paseo del Mar coastal areas from the southwestern Gulf of Mexico. Marine and Petroleum Geology. 110, 650-675.

Romans, B.W., Castelltort, S., Covault, J.A., Fildani, A., Walsh, J.P. 2016. Environmental signal propagation in sedimentary systems across timescales. Earth-Science Reviews 153, 7–29.

Roser, B.P., Korsch, R.J., 1986. Determination of tectonic setting of sandstone-mudstone suites using SiO2 content and K2O/Na2O ratio. Journal of Geology 94, 635–650.

Sallam, E.S., Wanas, H.A., 2019. Petrography and geochemistry of the Jurassic siliciclastic rocks in the Khashm El-Galala area (NW Gulf of Suez, Egypt): implication for provenance, tectonic setting and source area paleoweathering. Journal of African Earth Sciences 160, 103607. https://doi.org/10.1016/j.jafrearsci.2019.103607.

Saylor, J. E., Jordan, J.C., Sundell, K.E., Wang, X.M., Wang, S.Q., Deng, T. 2018. Topographic growth of the Jishi Shan and its impact on basin and hydrology evolution, NE Tibetan PLateau. Basin Research 30, 544-563.

Shaanan, U., Rosenbaum, G. 2018. Detrital zircons as palaeodrainage indicators: Insights into southeastern Gondwana from Permian basins in eastern Australia. Basin Research, 30(S1), 36–47.

Sharman, G. R., Malkowski, M. A. 2020. Needles in a haystack: Detrital zircon U-Pb ages and the maximum depositional age of modern global sediment. Earth-Science Reviews 203, 103109. https://doi.org/10.1016/j.earscirev.2020.103109

Sircombe, K.N., 1999. Tracing provenance through the isotope ages of littoral and sedimentary detrital zircon, eastern Australia. Sedimentary Geology 124 (1–4), 47–67.

Solís-Alulima, B., Abati, J., Carmona, A.L., Alonso,G.G., Suárez, J.F., Stockli, D.F., 2022. Detrital zircon ages and provenance of a Cambrian succession in the Sierra Albarrana Domain (SW Iberian Massif). Lithos 408-409, 106542. https://doi.org/10.1016/j.lithos.2021.106542

Tan, M. X., Zhu, X. M., Liu, W., Han, X. F. 2020. Sediment mixing of extrabasinal and intrabasinal sources in a narrow elongated half-graben? Constraints on provenance and seismic geomorphological analysis of the Upper Eocene Liaoxi Sag in the offshore northern Bohai Bay Basin (China). Journal of Petroleum Science and Engineering 193, 107379. https://doi.org/10.1016/j.petrol.2020.107379.

Tan, M. X., Zhu, X. M., Liu, W., Tan, L.Y., Shi, R. S., Liu, C. N. 2018. Sediment routing systems in the second member of the Eocene Shahejie Formation in the Liaoxi Sag, offshore Bohai Bay Basin: A synthesis from tectono-sedimentary and detrital zircon geochronological constraints. Marine and Petroleum Geology 94, 95-113.

Tang, J.Z., Zhang, Z.C., Xue, J.Z., Liu, B., Chen, Y., Zhang, S.H. 2021. Permo-Carboniferous provenance shifts at the northern margin of the North China Craton and their tectonic implications: Detrital zircon U–Pb–Hf records from central Inner Mongolia. Gondwana Research 95, 134-148.

Taylor, S.R., McLennan, S.M., 1985. The Continental Crust: Its Composition and Evolution. Blackwell Scientific Publications, United States (312 pp).

Thomson, K.D., Stockli, D.F., Clark, J.D., Puigdefàbregas, C., Fildani, A., 2017. Detrital zircon (U-Th)/(He-Pb) double-dating constraints on provenance and foreland basin evolution of the Ainsa Basin, south-central Pyrenees, Spain. Tectonics 36.

Toby, S.C., Duller, R.A., De Angelis S, Straub, K.M., 2019. A stratigraphic framework for the preservation and shredding of environmental signals. Geophysical Research Letters 46, 5837-5845.

Tyrrell, S., Haughton, P.D.W., Daly, J.S., Shannon, P.M., 2012. The Pb isotopic composition of detrital K-feldspar: a tool for constraining provenance, sedimentary processes and paleo-drainage. In: Sylvester, P. (Ed.), Quantitative Mineralogy and Microanalysis of Sediments and Sedimentary Rocks, vol. 42. Mineralogical Association of Canada Short Course Series, pp. 203-217.

Vermeesch, P., 2013. Multi-sample comparison of detrital age distributions. Chemical Geology 341, 140-146.

Wanas, H.A., Assal, E.M., 2021. Provenance, tectonic setting and source area-paleoweathering of sandstones of the Bahariya Formation in the Bahariya Oasis, Egypt: An implication to paleoclimate and paleogeography of the southern Neo-Tethys region during Early Cenomanian. Sedimentary Geology 413, 105822.

Wang, A., Yang, D., Yang, H., Mu, M., Quan, Y., Hao, L., Xu, W., 2021a. Detrital zircon geochronology and provenance of sediments within the Mesozoic basins: new insights into tectonic evolution of the Qinling Orogen. Geoscience Frontiers 12, 101107 https://doi.org/10.1016/j.gsf.2020.11.004.

Wang, R., Ji, Y.L., Colombera, L., Mountney, N.P., Yuan, B., Li, D.J., Song, H.Y., Zhou, S. 2021b. Axial and transverse depositional systems of a syn-rift basin fill (Bohai Bay Basin, China). Marine and Petroleum Geology 128, 105045. https://doi.org/10.1016/j.marpetgeo.2021.105045

Wang, C., Song, S.G., Su, L., Allen, M.B. 2022. Crustal maturation and cratonization in response to Neoarchean continental collision: The Suizhong granitic belt, North China Craton. Precambrian Research 377, 106732. https://doi.org/10.1016/j.precamres.2022.106732

Wissink, G.K.，Wilkinson, B.H.，Hoke, G. D., 2018, Pairwise sample comparisons and multidimensional scaling of detrital zircon ages with examples from the North American platform, basin, and passive margin settings. Lithosphere 10, 478-491.

Wood, G.D., Gabriel, A.M., Lawson, J.C., 1996, Palynological Techniques – Processing and Microscopy. In: Jansonius, J., MacGregor, D.C. (Eds.), Palynology: Principles and Applications 1. American Association of Stratigraphic Palynologists Foundation, pp. 29–50.

Wu, X.L., 2013. Reservoir-forming Conditions & Resource Potential of Palaeogene Shale Oil from the South of Bohai Bay Basin. China Univ. Geoseosci (Doctoral Degree Thesis in Chinese with English

Abstract).

Wu, Z.P., Zhang, L., Li, W., Gao, Y. J., Jia, H. B., 2012. Early Paleogene (Ek-Es4x) structure framework restoration of Dongying sag. Journal of China University of Petroleum. 36, 13-19. (In Chinese with English Abstract)

Wu, Q.R., Xian, B.Z., Gao, X.Z., Bai, Q.L., Wang, Z., Liu, J.P., Chen, P., Li, Y.Z., Rahman, N.U., Tian, R.H., Zhang, W.M., Zhang, H.Z. 2022. Differences of sedimentary triggers and depositional architecture of lacustrine turbidites from normal regression to forced regression: Eocene Dongying depression, Bohai Bay Basin, East China. Sedimentary Geology 439, 106222. https://doi.org/10.1016/j.sedgeo.2022.106222

Xu, J.Q., Li, Z. 2015. Middle–Late Mesozoic sedimentary provenances of the Luxi and Jiaolai areas: Implications for tectonic evolution of the North China Block. Journal of Asian Earth Sciences 111, 284-301.

Xu, J.Q., Li, Z., Shi, Y.H., 2013. Jurassic detrital zircon U–Pb and Hf isotopic geochronology of Luxi Uplift, eastern North China, and its provenance implications for tectonic-paleogeographic reconstruction. Journal of Asian Earth Sciences 78, 184–197.

Xu, W., Liu, F.L. 2019. Geochronological and geochemical insights into the tectonic evolution of the Paleoproterozoic Jiao-Liao-Ji Belt, Sino-Korean Craton. Earth-Science Reviews 193, 162-198.

Yang, F., Santosh, M., Kim, S. W., Zhou, H. Y. 2021. Late Neoarchean to Paleoproterozoic arc magmatism in the Shandong Peninsula, North China Craton and its tectonic implications. Precambrian Research 358, 106188. https://doi.org/10.1016/j.precamres.2021.106188

Yang, J. H., Wen, H. J., Guo, X. Z., Luo, C. G., Yu, W. X., Du, S. J., Cui, Y. 2022. Detrital zircon U-Pb ages and trace elements indicate the provenance of Early Carboniferous Li–rich claystone from Central

Guizhou, South China. Sedimentory Geology 442, 106278. https://doi.org/10.1016/j.sedgeo.2022.106278.

Yang, J. H., Wu, Y. F., Shao, J. A., Wilde, S. A., Xie, L. W., Liu, X. M. 2006. Constraints on the timing of uplift of the Yanshan Fold and Thrust Belt, North China. Earth and Planetary Science Letters 246, 336-352.

Zhang, L., Wu, Z. P., Li, W., Wang, G. Z., Zhang, Q., Jia, H. B., Dai, L. 2012. Development Characteristics and Quantification of Pingnan-Shicun Transfer Structures in Dongying Sag. Geological Journal of China Universities 18, 365-371. (In Chinese with English Abstract)

Zhang, S.H., Zhao, Y., Song, B., Hu, J.M., Liu, S.W., Yang, Y.H., Chen, F.K., Liu, X.M., Liu, J., 2009. Contrasting Late Carboniferous and Late Permian-Middle Triassic intrusive suites from the northern margin of the North China Craton: Geochronology, petrogenesis, and tectonic implications. Geological Society of America Bulletin 121, 181–200.

Zhang, Y. Q., Qiu, E. K., Dong, S. W., Li, J. H., Shi, W. 2022. Late Mesozoic intracontinental deformation and magmatism in North and NE China in response to multi-pLate convergence in NE Asia: An overview and new view. Tectonophysics 835, 229377. https://doi.org/10.1016/j.tecto.2022.229377.

Zhai, M.G., Zhang, Y.B., Li, Q.L., Zou, Y., He, H.L., Shan, H.X., Liu, B., Yan, C.L., Liu, P., 2021. Cratonization, lower crust and continental lithosphere. Acta Petrol. Sin. 37, 1–23 (in Chinese with English abstract).

Zhou, Y.Y., Zhai, M.G. 2022. Mantle plume-triggered rifting closely following Neoarchean cratonization revealed by 2.50–2.20 Ga magmatism across North China Craton. Earth-Science Reviews 230, 104060. https://doi.org/10.1016/j.earscirev.2022.104060.

Zhu, X.M., Li, S.L., Liu, Q.H., Zhang, Z.L., Xu, C.G., Du, X.F., Li, H.Y., Shi, W.L., 2017. Source to sink studies between the Shaleitian uplift and surrounding sags: perspectives on the importance of hinterland relief and catchment area for sediment budget, Western Bohai Bay Basin, China. Interpretation 5, ST65–ST84.

Zhu, Y.B., Liu, S.F., Zhang, B., Gurnis, M., Ma, P.F. 2021. Reconstruction of the Cenozoic deformation of the Bohai Bay Basin, North China. Basin Research 33, 364-381.

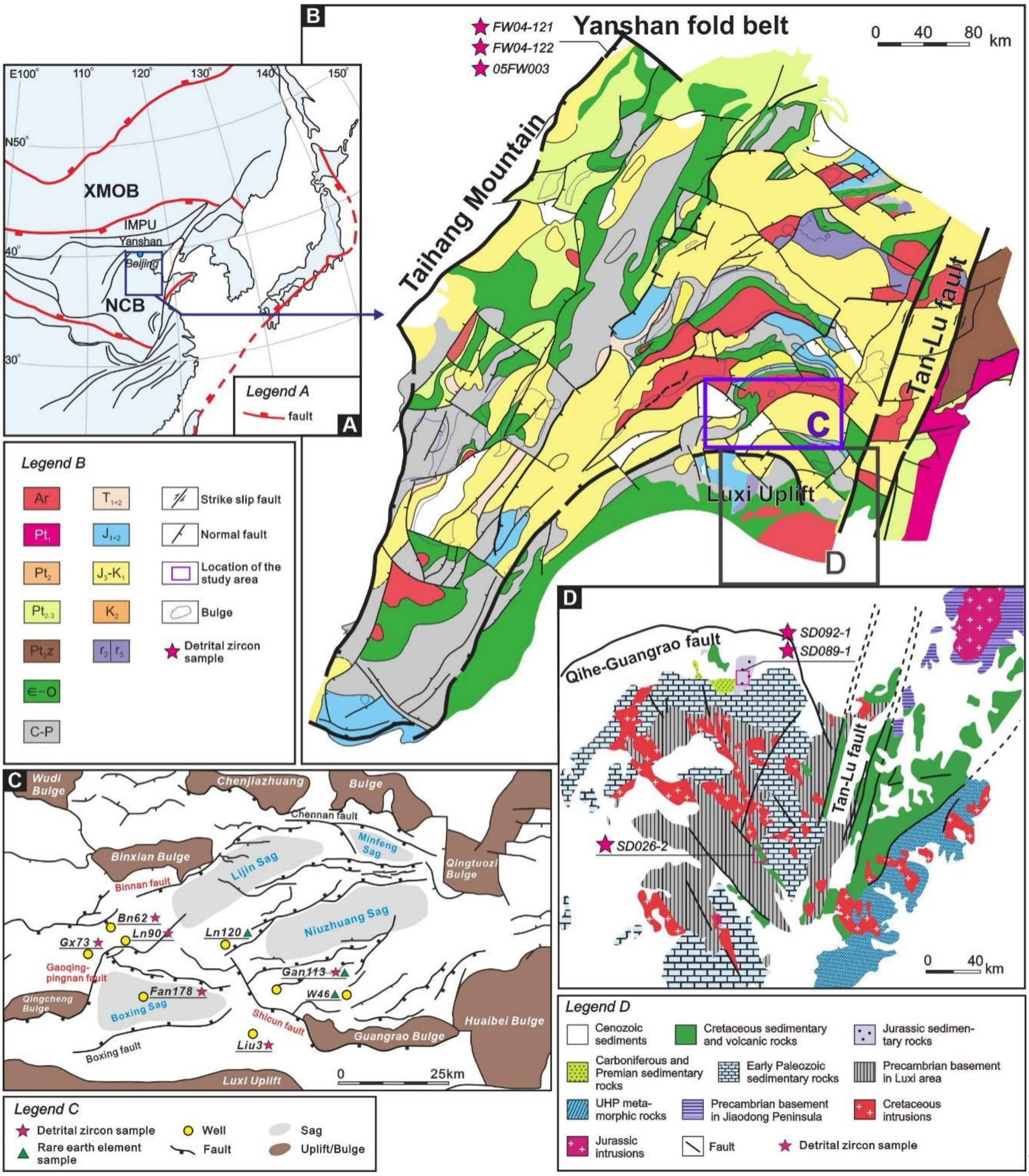

Fig. 1. (A) Regional tectonic setting (modified from Xu et al. (2015), in which the NCB, IMPU, XMOB respectively denote the North China Block, Inner Mongolia Paleo-uplift, Xing-Meng Orogenic Belt. (B) The Cenozoic basement of Bohai Bay Basin (modified from Qi et al., 2004). (C) Schematic map of secondary tectonic units in the Dongying Depression (modified from Meng et al., 2021) and the location of the samples from Yanshan fold belt (Yang et al., 2006) and Luxi area (Xu et al., 2013, 2015). (D) Geologic map of Luxi and adjacent areas (modified from Xu et al., 2015).

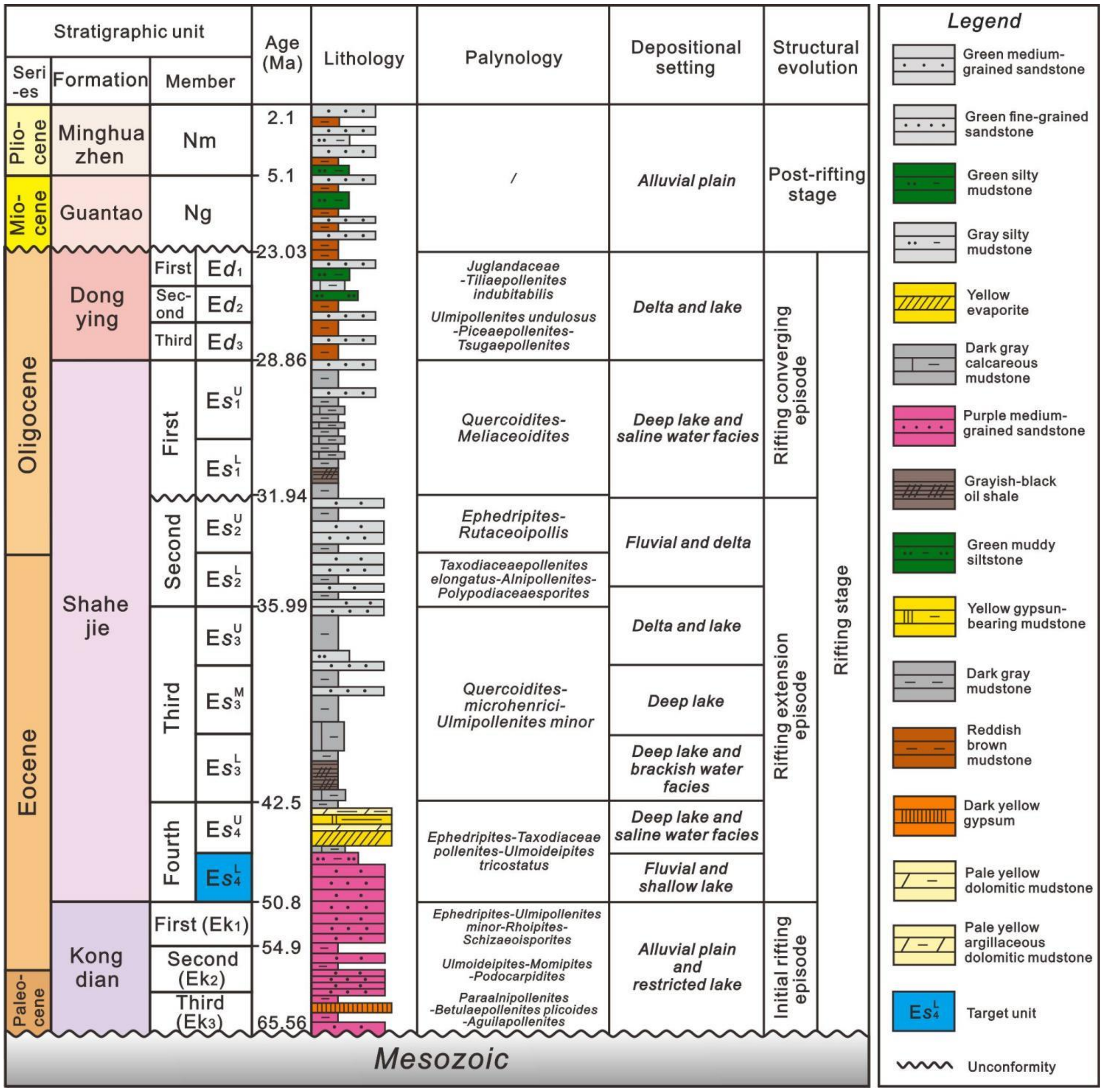

Fig. 2. Stratigraphic column and stratigraphic framework of the Dongying Depression. Modified after He et al. (2017) and Liu et al. (2018).

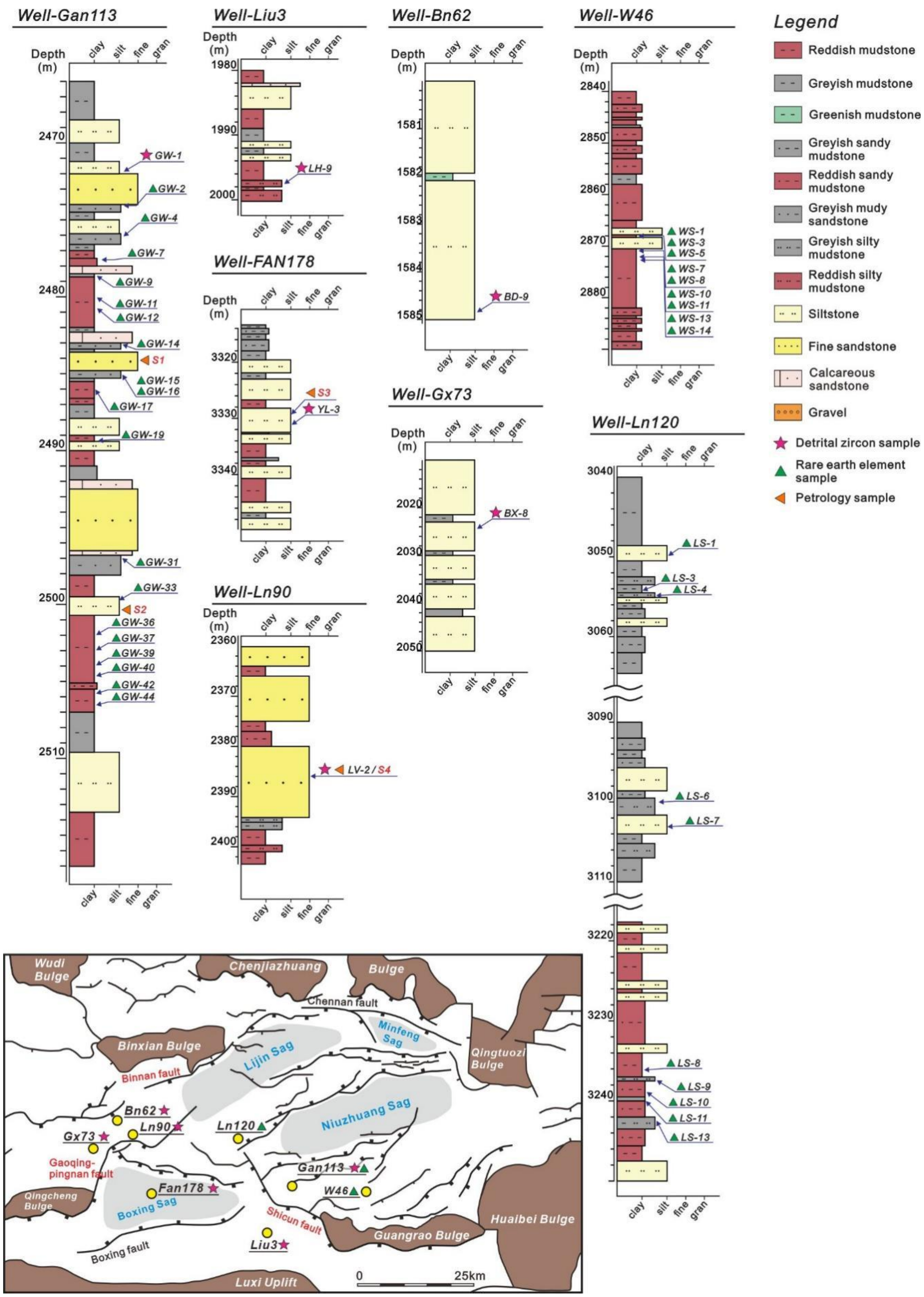

Fig. 3. Schematic lithologic sections from study wells of the Dongying Depression from the Lower 4th member of the Shahejie Formation. The map is modified from Meng et al. (2021).

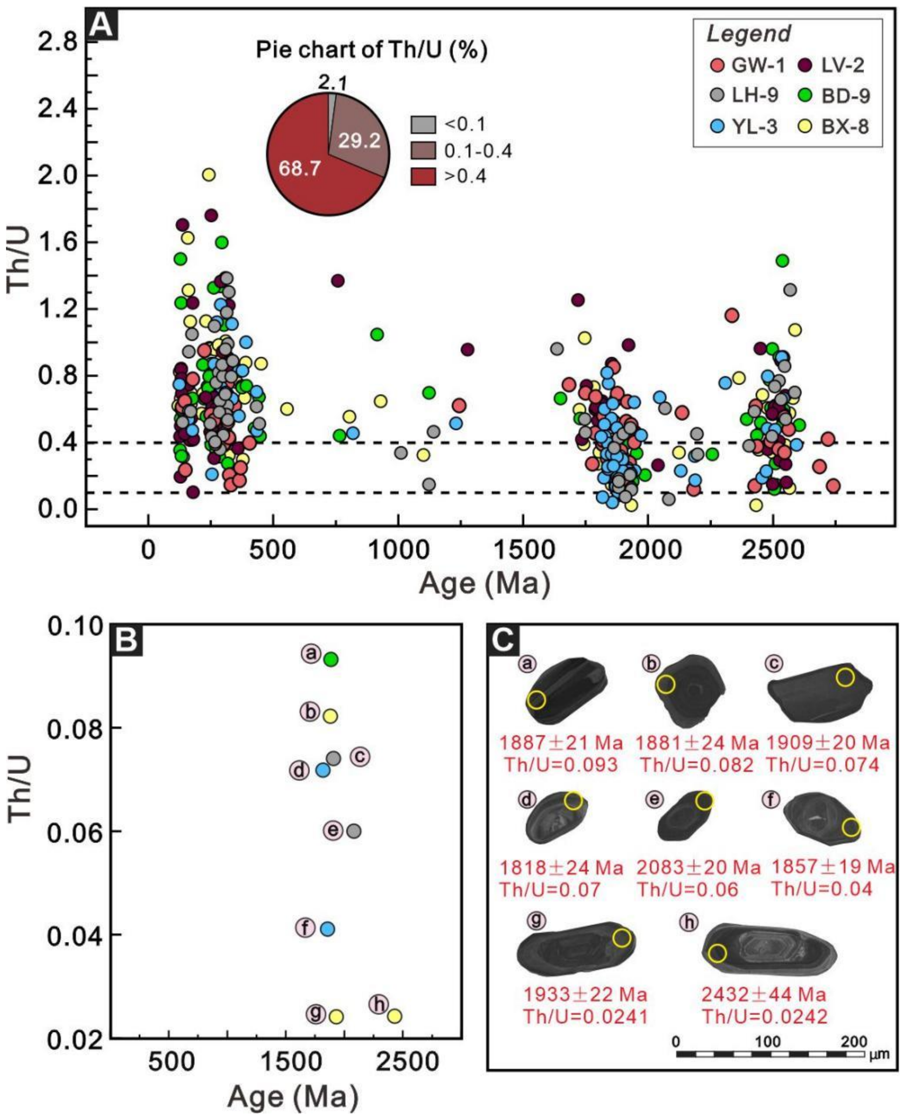

Fig. 4. (A) Th/U and its percentage of zircon grains in the sand samples from the Lower 4th member of Shahejie Formation. (B) Scatter diagram with Th/U<0.1. (C) Representative examples of the morphology and internal structure of zircon grains with Th/U<0.1. The Th/U ratios are reported in supplementary material 1. The origin of samples reported in the legend is shown in Fig. 3.

Fig. 5. Representative examples of the morphology and internal structure of zircon grains from the sand samples of the Dongying Depression; all to the same scale. The origin of samples is shown in Fig. 3.

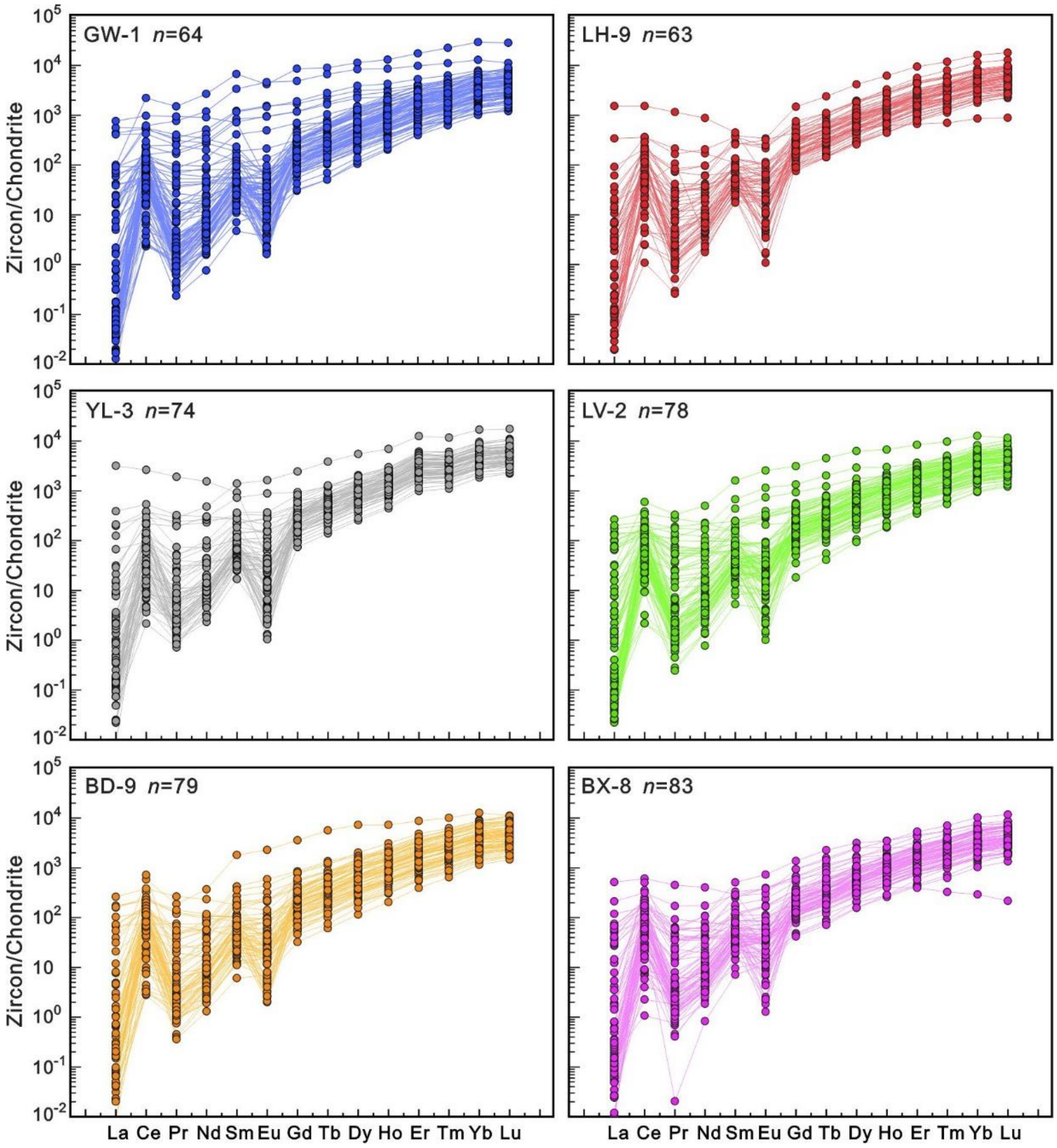

Fig. 6. Chondrite-normalized REE patterns of detrital zircons of the Dongying Depression; normalization is performed according to values from Taylor and McLennan (1985).

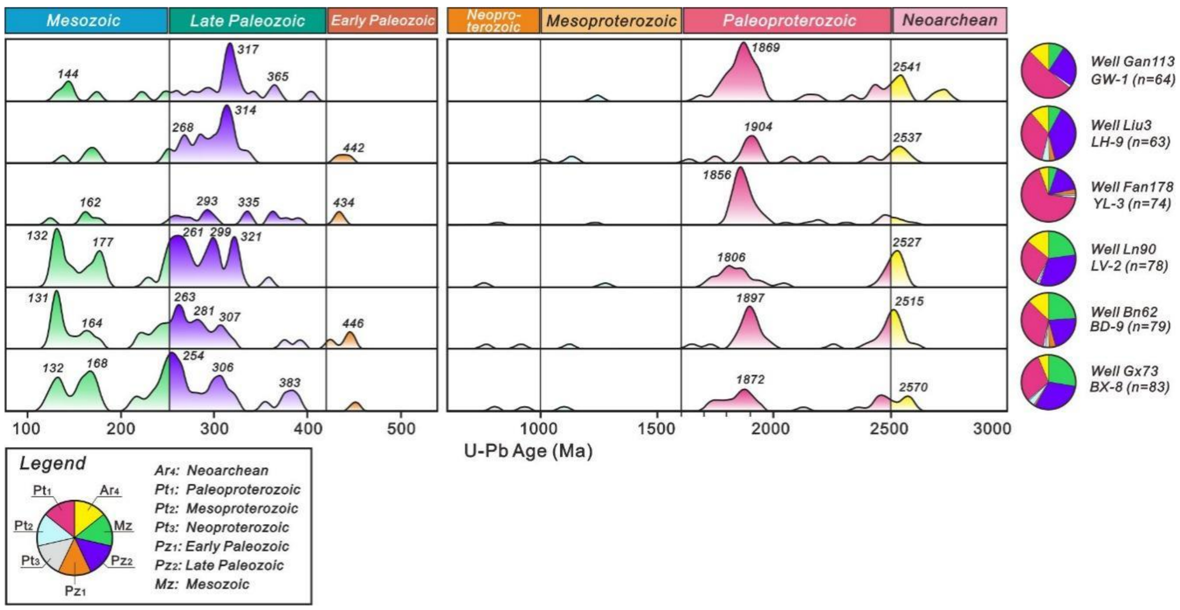

Fig. 7. Normalized U-Pb detrital zircon age Kernel Density Estimates (KDEs) of all samples of this study (n = amount of near concordant age determinations / amount of analysed U-Pb compositions) and their proportions shown in pie charts. The U-Pb ages are reported in supplementary material 1.

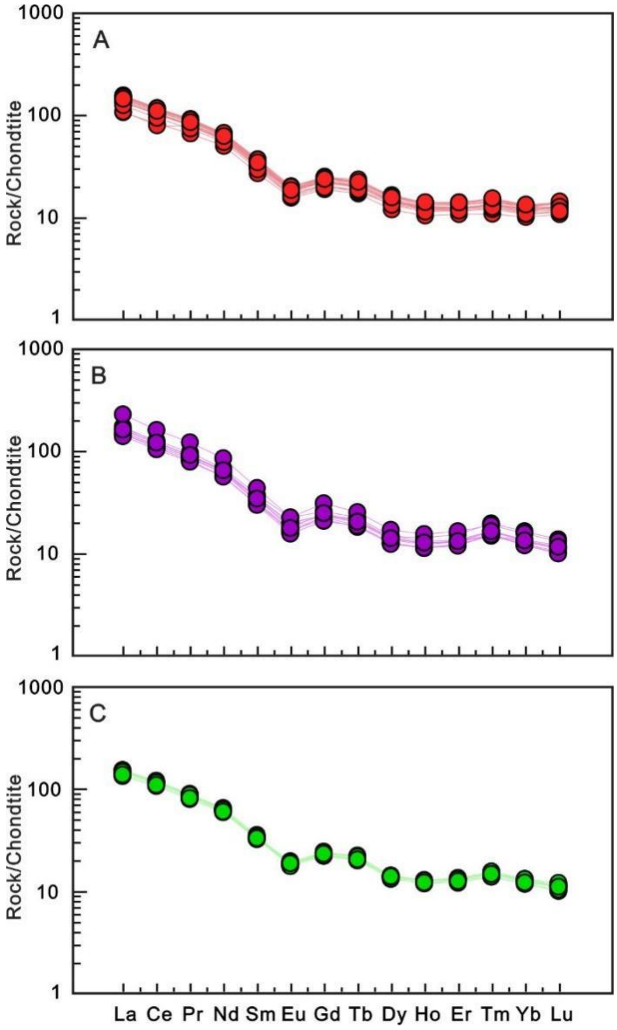

Fig. 8. REE diagrams, normalized to chondrite according to values from Taylor and McLennan (1985).

(A) Well Gan113; (B) Well Ln120; (C) Well W46.

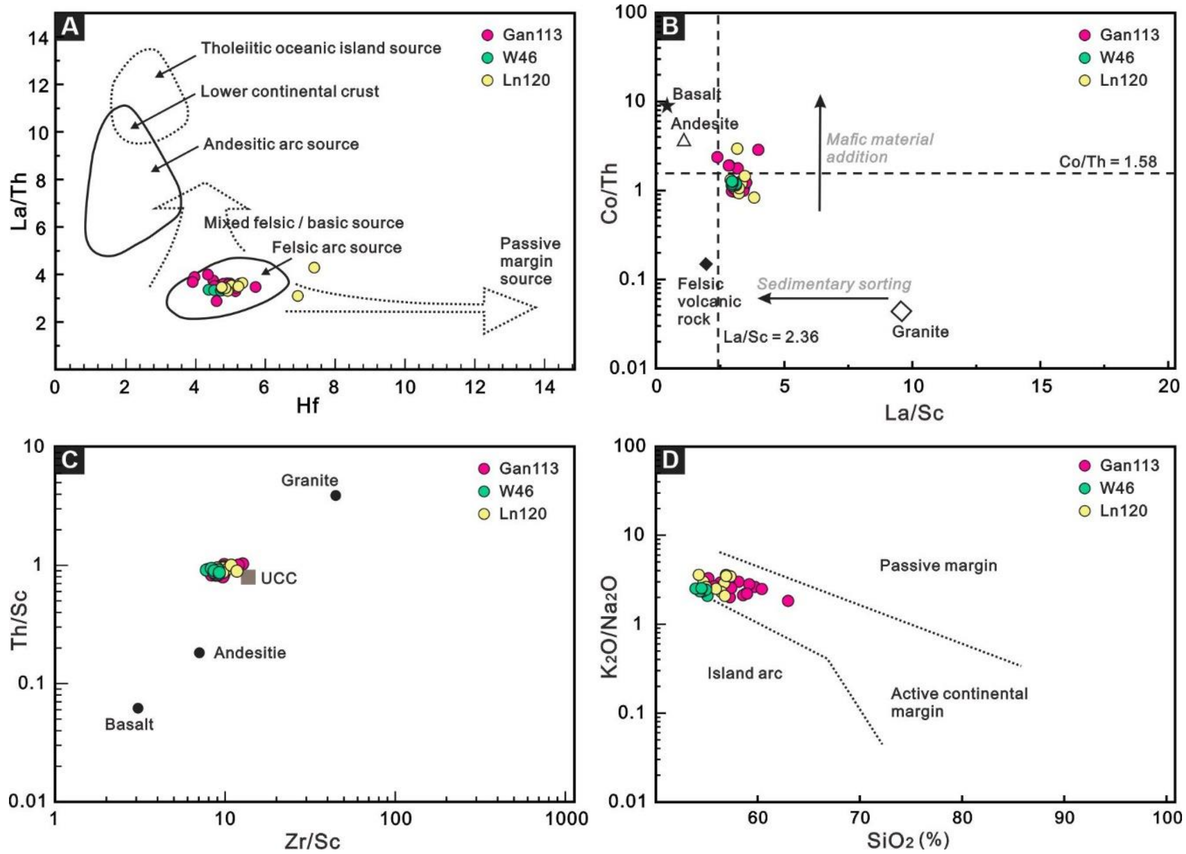

Fig. 9. Provenance-dependent elements and elemental ratios for the Lower 4th member of the Shahejie Formation mudstones: (A) La/Th vs. Hf diagram (after Floyd and Leveridge, 1987); (B) La/Sc vs. Co/Th diagram (after McLennan et al., 1993). (C) Zr/Sc vs. Th/Sc diagram (after McLennan et al., 1993) and (D) SiO_2 vs. K_2O/Na_2O diagram (after Roser and Korsch, 1986). Spots color-coded according to borehole name, as in Fig. 3.

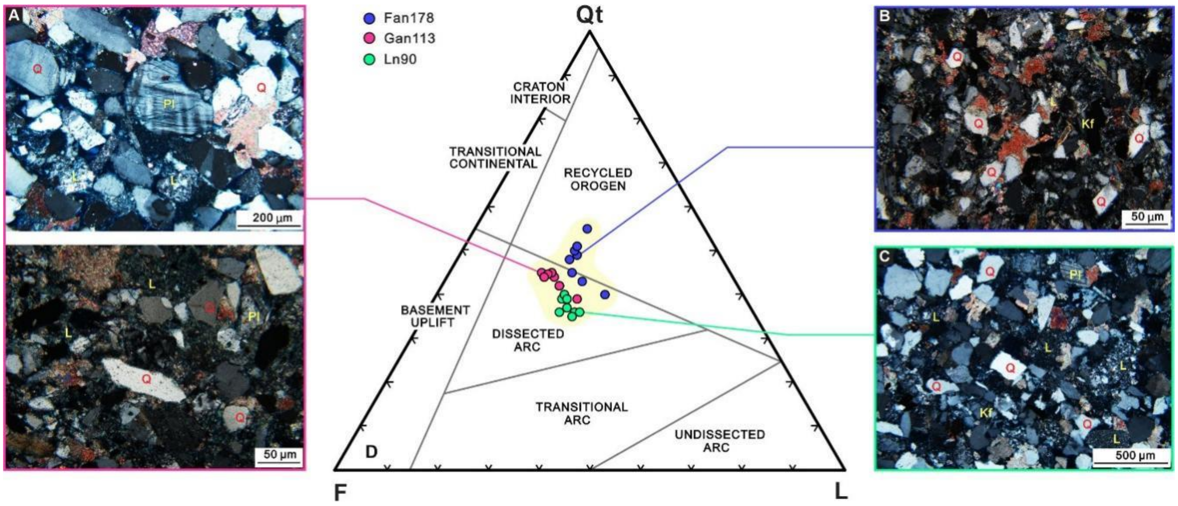

Fig. 10. Photomicrographs of the collected sandstone samples and discrimination plots of Qt–F–L. Fields after Dickinson (1985). Q, quartz; Pl, plagioclase; L, lithic fragments; Kf, K-feldspar; Qt, total quartz; F, total feldspars . Spots color-coded according to borehole name, as in Fig. 3.

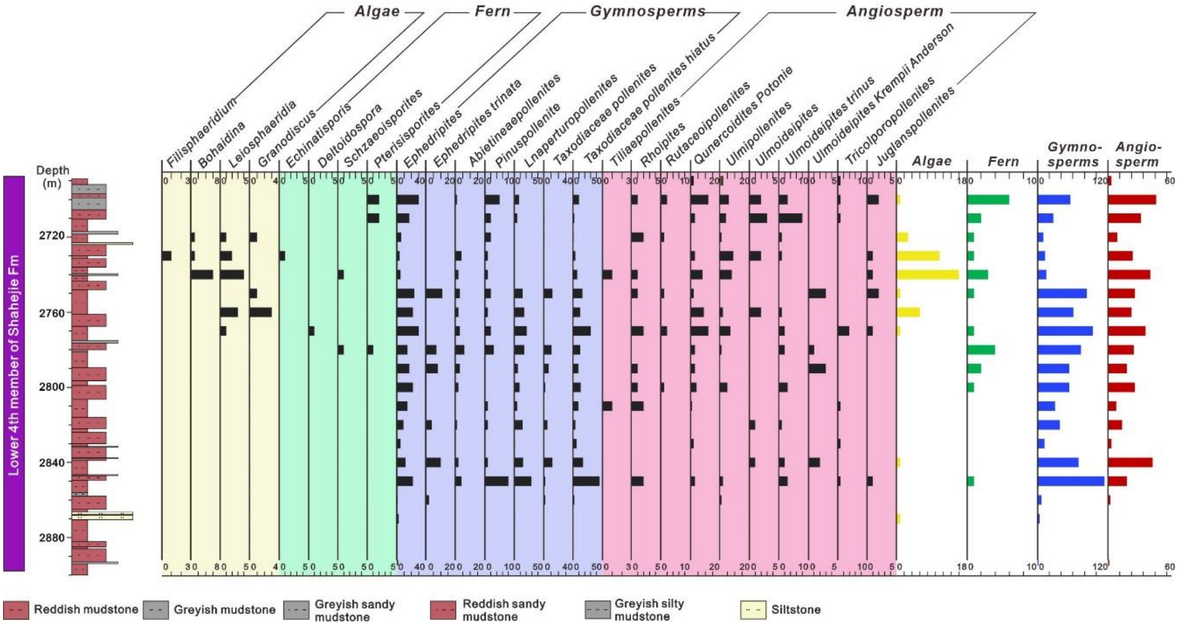

Fig. 11. Palynology of the Lower 4th member of the Shahejie Formation in the Dongying Depression from the well W46.

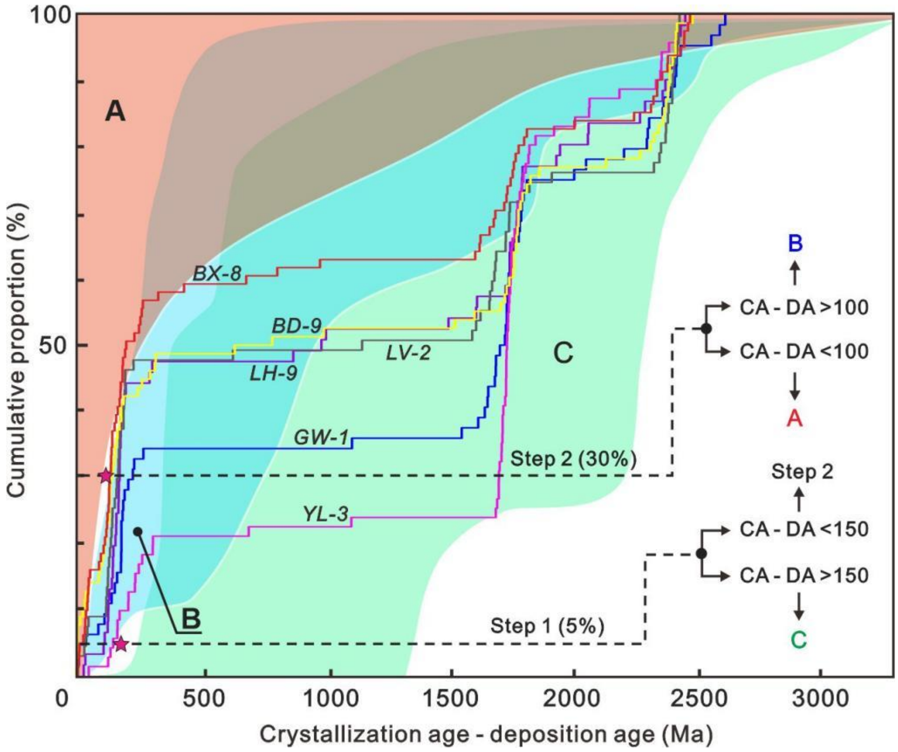

Fig. 12. Cumulative proportion curve of the difference between crystallization age (CA) and depositional age (DA) (modified from Cawood et al., 2012). A: convergent setting, B: collisional setting, C: extensional setting.

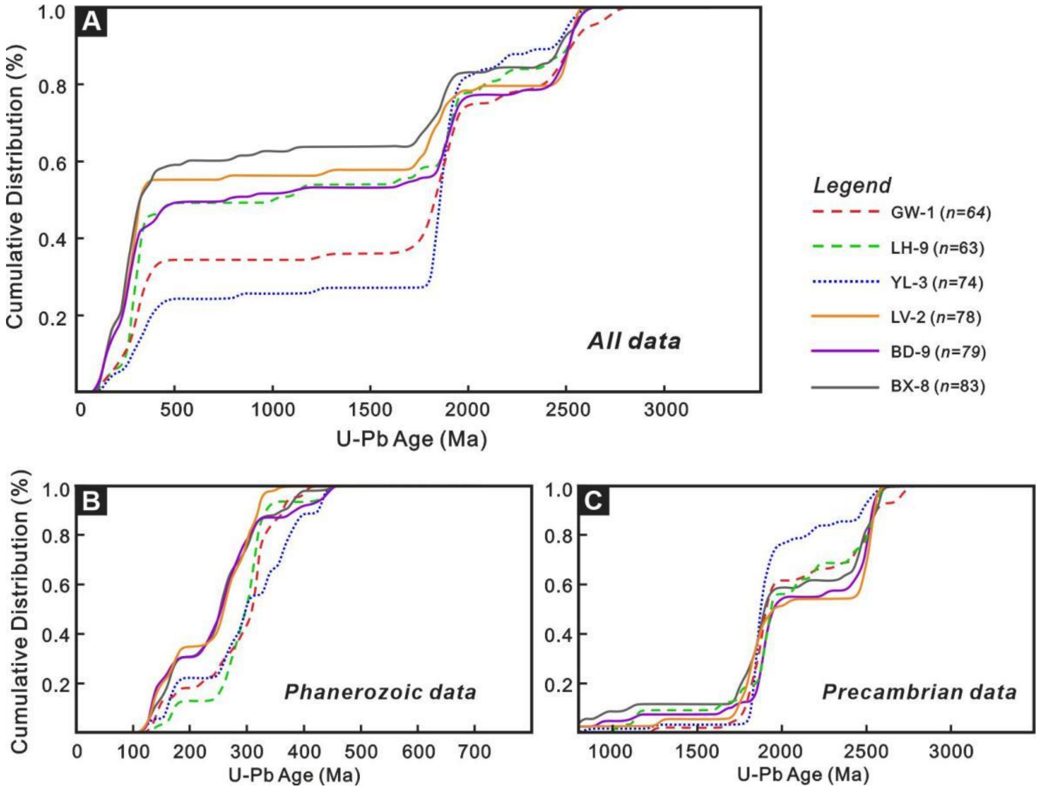

Fig.13. U–Pb age cumulative frequency plots. (A) All data; (B) Phanerozoic data; (D) Precambrian data.

Curves color-coded according to sample ID, as in Fig. 3.

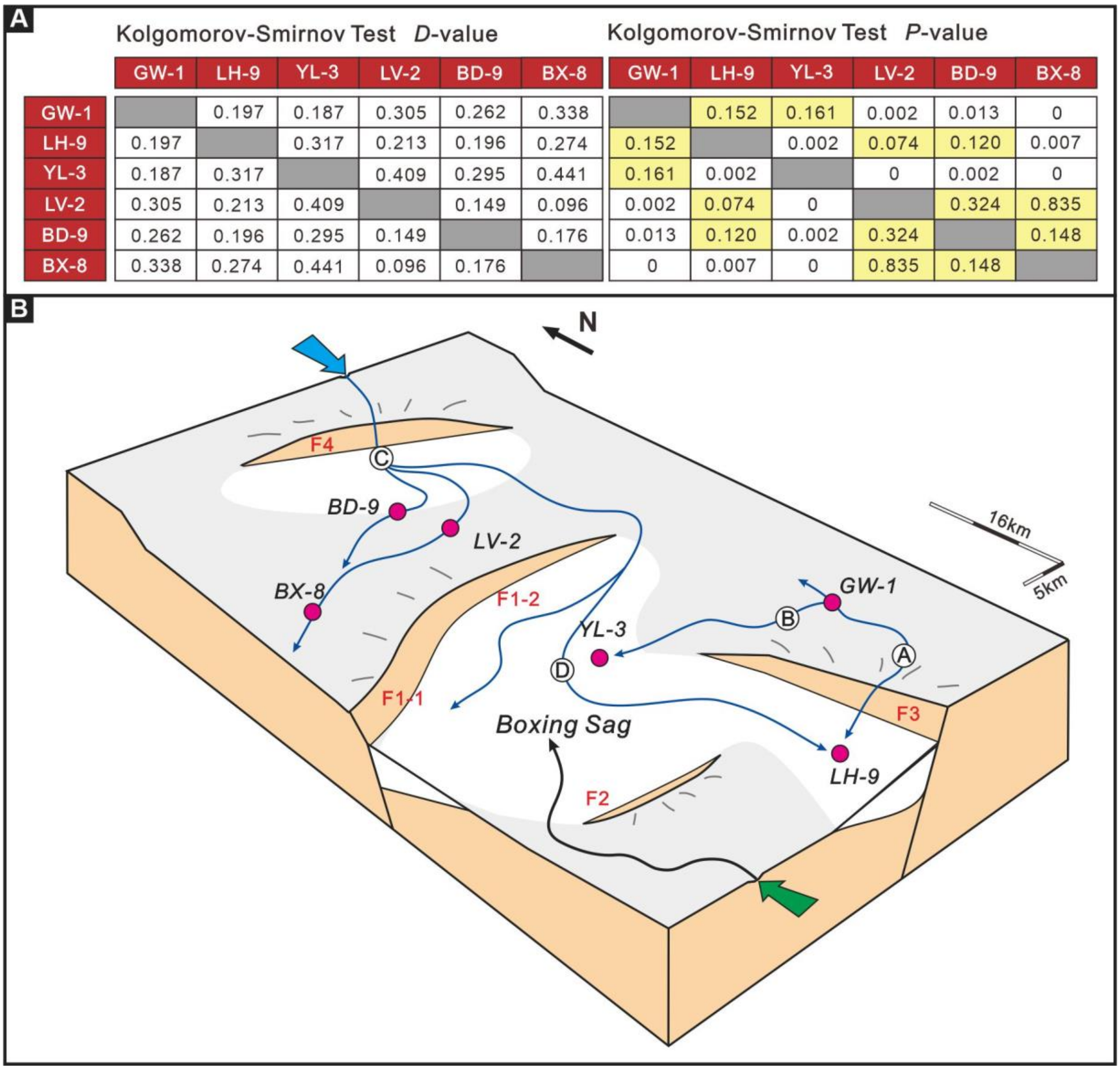

A

Kolgomorov-Smirnov Test *D*-value

	GW-1	LH-9	YL-3	LV-2	BD-9	BX-8
GW-1		0.197	0.187	0.305	0.262	0.338
LH-9	0.197		0.317	0.213	0.196	0.274
YL-3	0.187	0.317		0.409	0.295	0.441
LV-2	0.305	0.213	0.409		0.149	0.096
BD-9	0.262	0.196	0.295	0.149		0.176
BX-8	0.338	0.274	0.441	0.096	0.176	

Kolgomorov-Smirnov Test *P*-value

	GW-1	LH-9	YL-3	LV-2	BD-9	BX-8
GW-1		0.152	0.161	0.002	0.013	0
LH-9	0.152		0.002	0.074	0.120	0.007
YL-3	0.161	0.002		0	0.002	0
LV-2	0.002	0.074	0		0.324	0.835
BD-9	0.013	0.120	0.002	0.324		0.148
BX-8	0	0.007	0	0.835	0.148	

Fig. 14. Results of the K–S (Kolmogorov-Smirnov) test (A) and sediment routing system of the early Eocene in the Dongying Depression (B). Sample IDs as in Fig. 3.

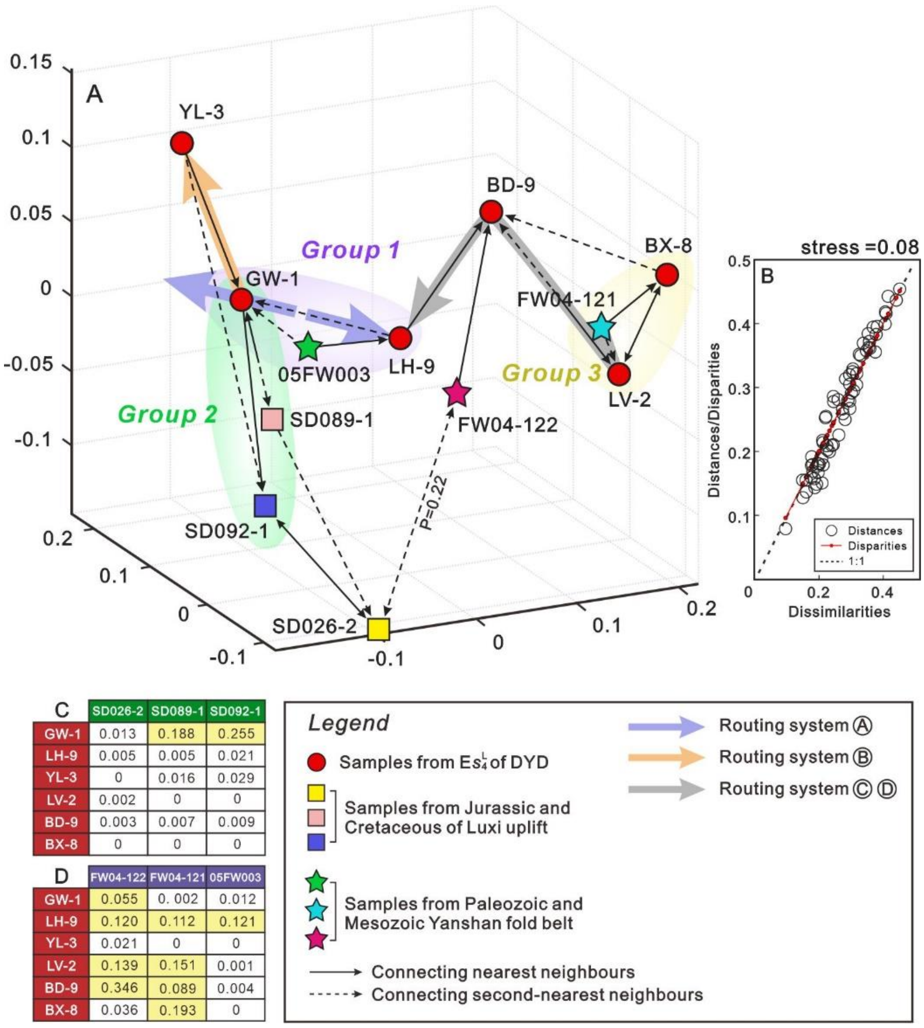

C	SD026-2	SD089-1	SD092-1
GW-1	0.013	0.188	0.255
LH-9	0.005	0.005	0.021
YL-3	0	0.016	0.029
LV-2	0.002	0	0
BD-9	0.003	0.007	0.009
BX-8	0	0	0

D	FW04-122	FW04-121	05FW003
GW-1	0.055	0. 002	0.012
LH-9	0.120	0.112	0.121
YL-3	0.021	0	0
LV-2	0.139	0.151	0.001
BD-9	0.346	0.089	0.004
BX-8	0.036	0.193	0

Fig. 15. Summary of 3D-MDS results for detrital zircon U-Pb ages from the Dongying Depression, Luxi area, Yanshan fold belt (Yang et al., 2006; Xu et al., 2013, 2015). (A) and the Shepard plot with the 'stress value between 0.05 and 0.1' (B). This plot shows K-S dissimilarities between age samples (C and D) visualized in 3D space, where similar samples tend to be clustered and contrasting samples are spread apart (samples GW-1, LH-9, YL-3 are near the Shicun fault in the Dongying Depression; samples LV-2, BD-9, BX-8 are from northwest region in the Dongying Depression; samples SD026-2, SD089-1 and SD092-1 are from the Lower Cretaceous Mengyin Formation and the Middle-Upper Jurassic Santai Formation in the Luxi area; samples FW04-122, FW04-121 and 05FW003 are collected from the late Triassic-Early Cretaceous sandstone and Carboniferous-late Permian sandstone in the Yanshan fold belt).

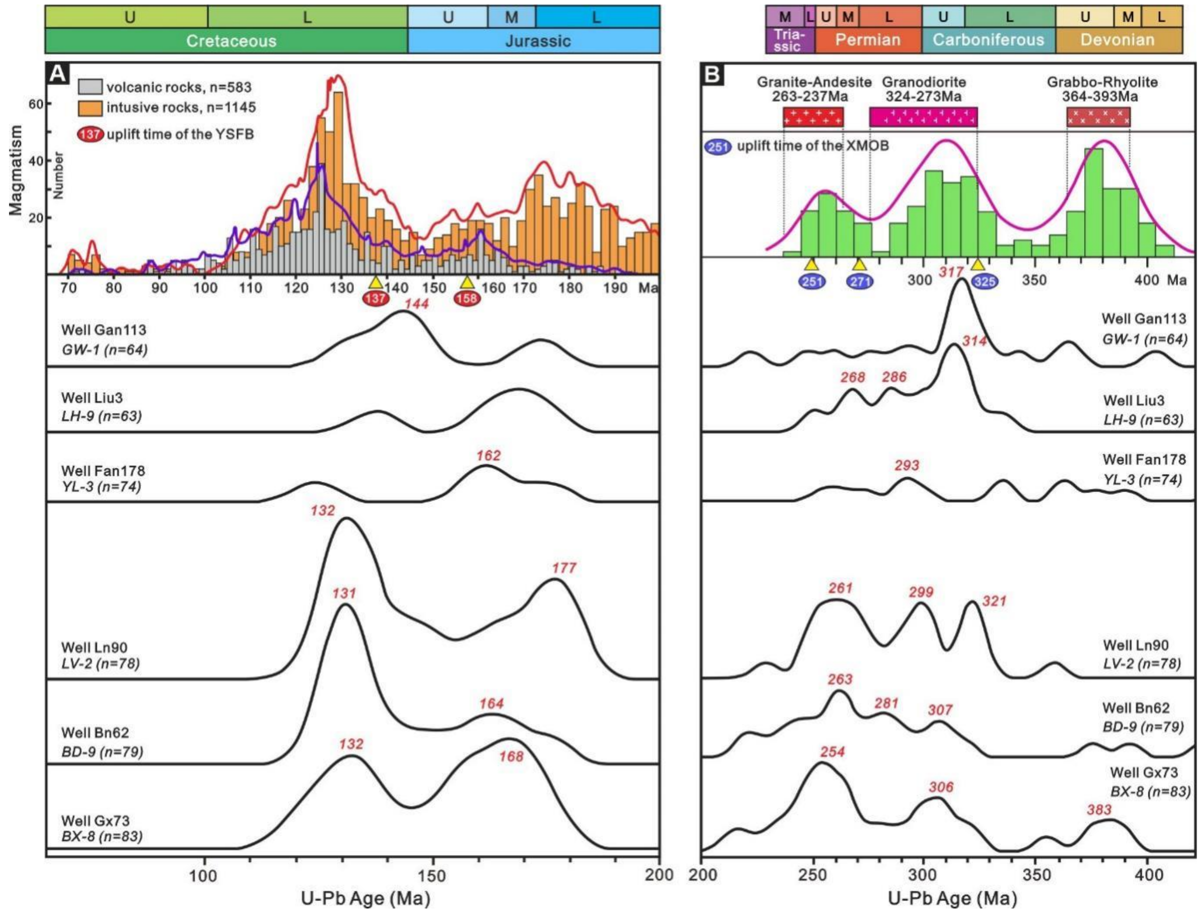

Fig. 16. Comparison of Jurassic-Cretaceous (A) (Zhang et al., 2022) and Devonian-middle Middle Triassic (B) (Ma et al., 2014) magmatism in the North China Craton with the early Eocene detrital zircon records from the Dongying Depression.

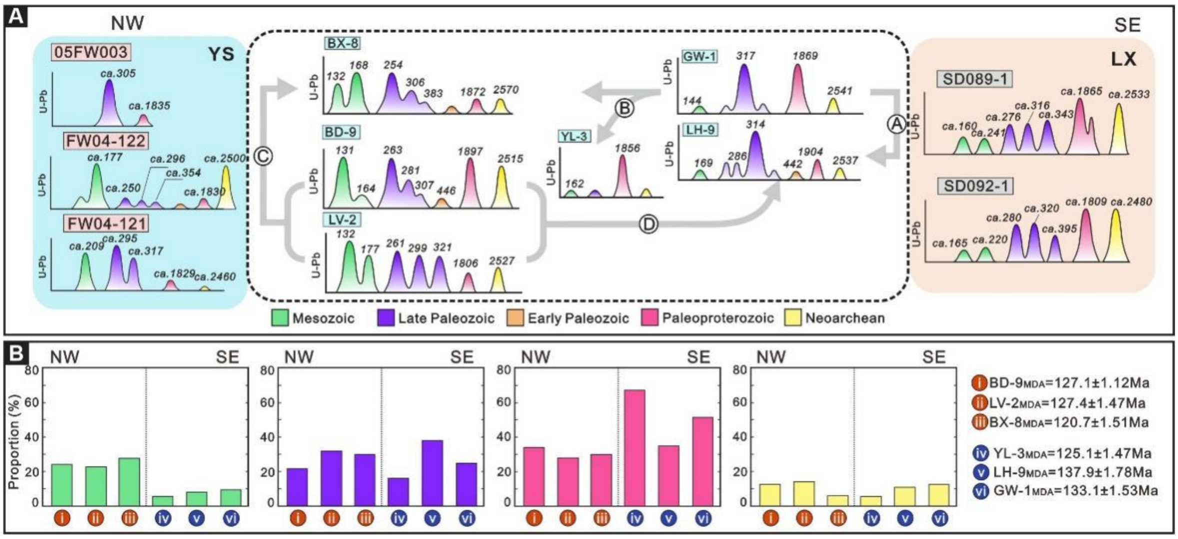

Fig. 17 . (A) Differential response of provenance signals of different sediment paths in the early Eocene Dongying Depression, compared with Yanshan and Luxi area (Yang et al., 2006; Xu et al., 2013, 2015); (B) Comparison of the proportion of provenance signals in each sample (i-iii refers to samples on the south side of Binnan fault, and iv-vi refers to samples on the periphery of Shicun fault). Sample IDs as in Fig. 3.

Table 1. Information of analyzed detrital zircon samples. See Fig. 1 for well location and Fig. 3 for sample intervals in each well.

Region	Well	Sample	Sample type	Strata	Number of analyses
East side of Shicun fault	Gan113	GW-1	Sandstone from core	Es_4^L	64
West side of Shicun fault	Liu3	LH-9	Sandstone from core	Es_4^L	63
Boxing Sag	Fan178	YL-3	Sandstone from core	Es_4^L	74
	Ln90	LV-2	Sandstone from core	Es_4^L	78
South side of Binnan Fault	Bn62	BD-9	Sandstone from core	Es_4^L	79
	Gx73	BX-8	Sandstone from core	Es_4^L	83

Table 2. Values of detrital zircon age and percentage of effective grains from study wells in the Dongying Depression.

(A) Phanerozoic	Empty Cell	Empty Cell	Empty Cell	Empty Cell	Empty Cell	Empty Cell	Empty Cell	Empty Cell	Emp Cell
			Percentage of total effective grains						
Well	Sample	Grains	Mesozoic			Late Paleozoic			Earl
			Cretaceous	Jurassic	Triassic	Permian	Carboniferous	Devonian	Silu
			66–145	145–201	201–252	252–299	299–359	359–419	419-
Gan113	GW-1	64	4.69 %(3)	1.56 %(1)	3.13 %(2)	6.25 %(4)	14.06 %(9)	4.69 %(3)	0

(A) Phanerozoic	Empty Cell	Empty Cell	Empty Cell	Empty Cell	Empty Cell	Empty Cell	Empty Cell	Empty Cell	Emp Cell
			9.4 % (6)			25 % (16)			0
Liu3	LH-9	63	1.59 %(1)	4.76 %(3)	1.59 %(1)	15.87 %(10)	22.22 %(14)	0	1.59
			7.94 %(5)			38.09 %(24)			3.18
Fan178	YL-3	74	1.35 %(1)	4.05 %(3)	0	6.76 %(5)	4.05 %(3)	5.41 %(4)	2.70
			5.4 %(4)			16.22 %(12)			2.70
Ln90	LV-2	78	8.97 %(7)	10.26 %(8)	3.85 %(3)	19.23 %(15)	12.82 %(10)	0	0
			23.08 %(18)			32.05 %(25)			0
Bn62	BD-9	79	10.13 %(8)	5.06 %(4)	8.86 %(7)	13.92 %(11)	5.06 %(4)	2.53 %(2)	2.53
			24.05 %(19)			21.71 %(17)			3.8 %
Gx73	BX-8	83	7.23 %(6)	10.84 %(9)	9.64 %(8)	15.66 %(13)	9.64 %(8)	4.82 %(4)	0
			27.71 %(23)			30.12 %(25)			1.20

(B) Precambrian

Well	Sample	Grains	Percentage of total effective grains			
			Precambrian			
			Neoproterozoic	Mesoproterozoic	Paleoproterozoic	Neoarchean
			539–1000	1000–1600	1600–2500	2500–2800

Gan113	GW-1	64	0	1.56 %(1)	51.56 %(33)	12.50 %(8)
Liu3	LH-9	63	0	4.76 %(3)	34.92 %(22)	11.11 %(7)
Fan178	YL-3	74	1.35 %(1)	1.35 %(1)	67.57 %(50)	5.41 %(4)
Ln90	LV-2	78	1.28 %(1)	1.28 %(1)	28.21 %(22)	14.10 %(11)
Bn62	BD-9	79	2.53 %(2)	1.27 %(1)	34.18 %(27)	12.66 %(10)
Gx73	BX-8	83	3.61 %(3)	1.20 %(1)	30.12 %(25)	6.02 %(5)

Table 3. Elemental ratios of our samples compared to the range of values of siliciclastic sediments derived from felsic and upper continental crust (UCC).

Elemental ratio of this study	**Studied samples**		**Range of sediments from felsic sources**[a]	**UCC**[b]
	Range	**Average**		
Eu/Eu*	0.57–0.71	0.65	0.40–0.94	0.72
La/Sc	2.38–3.99	3.16	2.50–16.3	2.21
Th/Sc	0.80–1.03	0.9	0.84–20.5	0.75
Cr/Th	5.10–12.06	6.25	4–15.0	8.76

a Cullers, 1994, Cullers, 2000; Cullers and Podkovyrov (2000).

b Rudnick and Gao (2003).

Table 4. Comparison of maximum depositional ages (MDA) between samples from different regions of the Dongying Depression.

Regin	Well	Sample	YSG / Ma	YC1σ(2+) / Ma	YC2σ(3+) / Ma
East side of Shicun fault	Gan113	GW-1	133.1 ± 1.53	144.4 ± 1.26	318.2 ± 1.12
West side of Shicun fault	Liu3	LH-9	137.9 ± 1.78	267.2 ± 1.3	268.0 ± 1.18
Boxing Sag	Fan178	YL-3	125.1 ± 1.47	162.1 ± 1.01	293.8 ± 1.83
	Ln90	LV-2	127.4 ± 2.55	129.7 ± 0.98	131.2 ± 0.83
Northwestern depression	Bn62	BD-9	127.1 ± 1.12	127.6 ± 0.87	129.2 ± 0.68
	Gx73	BX-8	120.7 ± 1.51	131.2 ± 1.3	132.3 ± 1.06